Physics – Uspekhi **68** (4) 327 – 356 (2025)

REVIEWS OF TOPICAL PROBLEMS PACS number: 96.30.Ys

ON THE 270th ANNIVERSARY OF M.V. LOMONOSOV MOSCOW STATE UNIVERSITY (MSU)

Novel views of asteroid activity: observations, models, forecasts

B.M. Shustov, V.V. Busarev, E.V. Petrova, M.P. Shcherbina, R.V. Zolotarev

DOI: https://doi.org/10.3367/UFNe.2024.08.039746

Contents

Abstract. Concepts of the fundamental difference between comets and asteroids have recently been significantly adjusted. Several dozen Main Belt asteroids have exhibited signs of cometary activity (comas, tails), earning the name "Main Belt comets." Using ground-based instruments, such active asteroids were detected primarily by imaging, so only the most pronounced manifestations of the activity of Main Belt asteroids have been observed. Undoubtedly, the number of asteroids with more moderate activity is incomparably larger. Detecting weak activity with ground-based instruments requires innovative approaches. The conventional method of broadband photometry and low-resolution spectroscopy turned out to be just such an effective tool. The use of this technique in [1–4] enabled a mass-scale study of a weak form of the activity of primitive-type asteroids, called sublimation-driven dust activity (SDA). SDA results in the formation of a temporary, fairly rarefied dust exosphere around the asteroid, detectable by broadband photometry. Modern concepts of active asteroids are reviewed. Attention is focused on manifestations of SDA and models of light scattering in dusty exospheres of asteroids. The mass character of SDA and its possible driving mechanisms are discussed.

Keywords: asteroids, active asteroids, sublimation activity, light scattering on dust particles, asteroid collisions

B.M. Shustov [(1,a)], **V.V. Busarev** [(1,2,b)], **E.V. Petrova** [(3,c)], **M.P. Shcherbina** [(1,d)], **R.V. Zolotarev** [(1,e)]
[(1)] Institute of Astronomy, Russian Academy of Sciences, ul. Pyatnitskaya 48, 119017 Moscow, Russian Federation
[(2)] Lomonosov Moscow State University, Sternberg State Astronomical Institute, Universitetskii prosp. 13, 119234 Moscow, Russian Federation
[(3)] Space Research Institute, Russian Academy of Sciences, ul. Profsoyuznaya 84/32, 117810 Moscow, Russian Federation
E-mail: [(a)] bshustov@inasan.ru, [(b)] busarev@sai.msu.ru, [(c)] epetrova@cosmos.ru, [(d)] morskayaa906@yandex.ru, [(e)] rv_zolotarev@mail.ru

Received 20 June 2024, revised 22 July 2024
Uspekhi Fizicheskikh Nauk **195** (4) 344 – 376 (2025)
Translated by M.Zh. Shmatikov

1. Active asteroids

1.1 Standard concepts of comets and asteroids as objects of a different nature

In the ancient science of astronomy, many definitions have been introduced over the millennia that seem clear to everyone, but still do not have 'official' (in astronomy, accepted by the International Astronomical Union) definitions, and are sometimes interpreted differently. Even the concept of a 'planet' was interpreted ambiguously until 2006. Resolution B5 of the General Assembly of the International Astronomical Union (IAU) provides definitions of the concepts of a 'planet' and 'dwarf planet'.[1] The concept of 'small bodies of the solar system' is also specified. These are objects that, according to their characteristics, cannot be classified either as dwarf planets or as planets or their satellites. It is explained that this group includes most asteroids of the solar system, most trans-Neptunian objects, comets, and other bodies.

Small bodies of the solar system also include meteoroids and interplanetary dust. Until recently, there was no clear criterion for distinguishing among the concepts of 'asteroid,'

[1] URL: https://www.iau.org/static/resolutions/Resolution_GA26-5-6.pdf. Accessed July 14, 2024.

'meteoroid,' and 'interplanetary dust.' In 2017, the IAU Commission F1 adopted recommendations on the use of the terms 'meteoroid' and 'interplanetary dust,'[2] allowing a more precise use of these terms. According to the adopted recommendations:

• meteoroids are solid objects measuring approximately 30 μm to 1 m, moving in interplanetary space;

• interplanetary dust is solid interplanetary objects up to 3 μm in size.

From the above definitions, it follows that asteroids (and comet nuclei) are solid bodies larger than 1 m.

Some terms are not explained in IAU resolutions, but in a glossary created by the IAU Office of Astronomy for Education. This is a joint project of the IAU Office of Astronomy for Education and the Max Planck Institute for Astronomy (Germany). The glossary[3] provides the following definitions (abridged):

• an asteroid is a member of an ensemble of relatively small (ranging in size from meters to many hundreds of kilometers) solid bodies of varying composition orbiting the Sun: some are rich in carbon, some contain more rocky material (silicates), and others consist mainly of metals. Many asteroids are gravitationally bound piles of rubble. Some asteroids have satellites — smaller asteroids orbiting them;

• a comet consists of a nucleus containing a mixture of various ices and rocky (dust) matter. Comet nuclei typically range in size from a few hundred meters to many tens of kilometers across. Most comets move in highly elliptical orbits. As a comet approaches the Sun, some of the surface ice evaporates, forming the characteristic outlines of the coma and tail. We see comets due to sunlight reflecting off the coma, tail, or (for comets far from the Sun) the nucleus. Comets are classified as short-period if their period is less than 200 years, and long-period (also called nonperiodic) otherwise.

The density of cometary nuclei, in cases where it has been measured with sufficient accuracy (usually in space experiments), is usually several times lower than that of asteroids. However, in dealing with small bodies, it is very problematic to determine their mass (and density), and it is difficult to apply this criterion to separate comets and small asteroids.

Usually, the difference in orbital characteristics is also mentioned: comet orbits are more elongated than those of asteroids. However, this difference is not absolute. As shown, for example, in [5–7], in the population of NEAs (near-Earth asteroids, i.e., asteroids with a perihelion distance $q < 1.3$ AU), many bodies in the process of relatively rapid dynamic evolution enter extremely elongated orbits and even collide with the Sun. According to study [7], which reports the results of integrating the movement of the NEA population over a time interval of 20 million years, the fraction of NEAs that collided with the Sun is about 15% of the total number of NEAs at the initial moment of time. On the other hand, in orbits with relatively small eccentricity and perihelion distances exceeding the ice boundary radius, there are many ice (ice-containing) bodies that do not manifest themselves as comets in any way, since they are always sufficiently far from the Sun.

[2] URL: https://www.iau.org/static/science/scientific_bodics/commissions/fl/meteordefinitions_approved.pdf. Accessed July 14, 2024.

[3] URL: https://astro4edu.org/resources/glossary/search/. Accessed July 14, 2024.

For quantitative classification of cometary and asteroid-type orbits, the so-called Tisserand parameter is used: a dynamic quantity that is approximately preserved when a small body approaches a planet. The Tisserand parameter — an approximate expression of the Jacobi constant for the restricted circular problem of three bodies (the Sun, the planet, and the small body) — makes it possible to relate the orbital elements of the small body after the encounter to the properties that existed before the encounter. Its value is preserved even in the case of close encounters [8]. The values of the Tisserand parameter for a small body differ depending on the planet. Since Jupiter is the most massive planet in the solar system and has the greatest dynamic influence on comets and asteroids, the most commonly used Tisserand parameter is the one calculated relative to Jupiter. It is denoted as $T_{\rm J}$. Here is an expression for the Tisserand parameter relative to Jupiter:

$$T_{\rm J} = \frac{a_{\rm J}}{a} + 2\left[(1-e^2)\,\frac{a}{a_{\rm J}}\right]^{1/2}\cos(i)\,, \tag{1}$$

where a, e, and i are the semi-major axis, eccentricity, and inclination of the orbit of the small body, respectively, and $a_{\rm J} = 5.2$ AU is the semi-major axis of Jupiter's orbit. As a first approximation, it is considered that, if $T_{\rm J} \gtrsim 3$, the body is an asteroid, and a comet if $T_{\rm J} \lesssim 3$.

The origin of asteroids and comets is also considered to be different. Asteroids are fragments of larger parent bodies that were broken up during mutual collisions. Many such bodies as early as during their formation (over the first few million years) underwent profound internal changes, including high-temperature differentiation of matter. The main source of heating was the decay of short-lived isotopes: ^{26}Al, ^{60}Fe, etc. (see [9–11]). Other parent bodies of asteroids, which initially included a significant proportion of ice, underwent only water differentiation (see, for example, [12]). Significant reserves of ice in bodies derived from this class of bodies, i.e., in asteroids of primitive (or low-temperature) types, could have survived to the present day due to high porosity and, consequently, low thermal conductivity of the surface layers, as follows from modeling [13, 14] and confirmed by observations, for example, in radiometric measurements of the surface characteristics of the C-type asteroid 162173 Ryugu made by the Hayabusa-2 space probe [15].

The predominant region of asteroid formation is the inner solar system, where they are concentrated in a toroidal structure — the Main Asteroid Belt (MAB).

Comets are found primarily in the region extending from the giant planets to the outer boundaries of the solar system. Comet nuclei are a large subset of ice-containing bodies — the 'heirs' of planetesimals (cometsimals) — that formed at the earliest stages of the formation of the solar system. The composition of cometary matter, especially in long-period comets, is close to the primary composition of planetesimals. However, the situation is not this simple. Some comets contain an intriguing combination of the most volatile ices from the most distant regions of the protoplanetary disk and high-temperature crystalline silicates from the inner edge of the protoplanetary disk [16, 17]. The presence of crystalline silicates in comets, revealed by infrared observations, has long been a mystery. Crystalline silicates are a surprise if comets are made of pristine interstellar material, since interstellar silicates are almost entirely amorphous. Heating to temperatures of > 1100 K may result in crystallization of silicates, but

no protoplanetary heating sources have been found that would be powerful enough to heat the materials in the outer zone of the protoplanetary disk to such high temperatures. This puzzle has hinted at a suggestion that large-scale mixing occurred in the protoplanetary disk.

In any case, the contents of volatiles in both classes of objects significantly differ, which provides the most obvious distinction between comets and asteroids.

1.2 Asteroid activity: manifestations

In recent years, the concepts of the fundamental difference between comets and asteroids have been significantly revised, and it has become clear that it is not always easy to distinguish a comet from an asteroid using the features listed in Section 1.1.

It has been known for a long time that bodies that are (or that were) considered to be asteroids can exhibit signs of cometary activity. According to [18], the first asteroid to show signs of cometary activity (a pronounced tail) was NEA 4015 Wilson–Harrington (Fig. 1, which is a detail of a frame taken from the ESO and Palomar Observatory archive[4]). However, study [19], which is referred to in [18], does not mention the asteroidal nature of the object. It is now believed that this is a near-Earth asteroid from the Apollo group, also known as comet 107P/Wilson–Harrington.

Astronomers now believe that comet-like activity, such as comas and tails, is not limited to comets. Over the past 70 years, about 30 such 'active asteroids' have been discovered, seven of which even have both cometary and asteroidal designations [18].

In 1996, the modern era of active asteroid exploration commenced with the discovery of an active object, 1/Elst–Pizarro, orbiting in the asteroid belt [20]. This object has repeatedly exhibited activity, especially near perihelion [21]. The repeated periodic activity in the perihelion zone, when the object is close to the Sun, is strong evidence that the activity is due to sublimation of ice, and this object was the first to be baptized a 'Main Belt Comet' (MBC). MBCs are a subset of active asteroids that orbit within the asteroid belt and exhibit activity driven primarily by sublimation (see [22] for a comprehensive review).

Based on the comet-like activity of several small asteroids, including two members of the Themis dynamical family, it was hypothesized that these bodies contain ice on/near the surface. In [23], such suggestions were confirmed for asteroid 24 Themis using spectroscopic infrared observations. The presence of surface ice on Themis was somewhat unexpected due to the relatively short lifetime of exposed ice at this distance ($\sim$ 3 AU) from the Sun.

Thus, with regard to the seemingly indisputable characteristic of comets — sublimation activity — the distinction between asteroids and comets has become considerably blurred in recent times. At the end of their active lives, some comets may look like asteroids when sublimation ceases due to the exhaustion of volatile material and/or the formation of a heat-insulating crust on their surface (see, e.g., [24]). Such a crust of refractory particles may eventually become so thick that subsurface volatiles cannot be heated to sublimation temperatures, even when passing perihelion at close distances to the Sun (well within the ice boundary). In [14], it is shown that, even with a long-term (more than 100 years) presence

[4] URL: https://www.eso.org/public/images/eso9212b/. Accessed July 14, 2024.

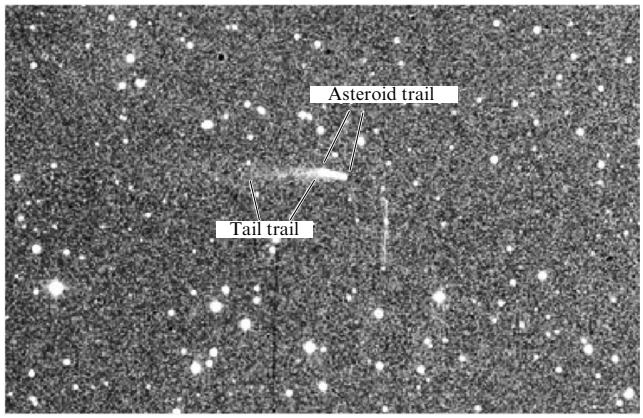

Figure 1. Image taken on November 19, 1949 (detail). Object 4015 Wilson–Harrington is shown with signs of activity (see explanations in text).

of a short-period comet in orbit (the example of comet 67P/Churyumov–Gerasimenko is considered), thermal energy accumulates in the subsurface layer of the nucleus with a thickness of no more than 10 m. The temperature distribution in this layer tends to a certain quasi-stationary state, which is maintained throughout the entire period of the comet's revolution in orbit. A similar result was obtained in [25], which modeled the thermal history of the surface layers of the object 11/2017 Ul (Oumuamua) during its flyby of the Sun and demonstrated the high survivability of subsurface ice. Another important result of this work is that, according to the model, the maximum temperature at a depth of 30 cm was noted not at perihelion but much later (100 days) after passing perihelion, and it never reached the sublimation temperature of H_2O ice, although, in perihelion, the surface temperature of the object exceeded 600 K. So, despite Oumuamua eventually being 'documented' as an asteroid, this does not imply that some amount of ice could not be contained beneath its surface.

In recent years, the concept of 'asteroid-comet continuum' has been increasingly used, meaning the absence of rigid boundaries between the properties of such objects. The term 'comet-asteroid continuum' (in recent years, the variant 'asteroid-comet continuum' has been used more frequently) was first introduced in [26], a popular presentation of the results of [23]. Various aspects of the asteroid-comet continuum are discussed in a number of studies (see, for example, [27–29]). The history of the issue can be traced in recent review [30], which presents a 2D diagram of the classification of small bodies by a dynamic parameter (Tisserand parameter T_J) and by an activity feature (detection of a coma). The diagram is presented in Fig. 2 (adapted from Fig. 1 [30]).

The diagram shows the region occupied by long-period comets (LPCs), which have $T_J < 2$ and orbital periods $P_{orb} \geqslant 200$ years; the region of Halley-type comets (HTCs), which have $T_J < 2$ and $P_{orb} < 200$ years; and the region of Jupiter-family comets (JFCs), which have $2 \leqslant T_J \leqslant 3$. The different orbital properties of these populations reflect their origin: LPCs originate from the Oort cloud; JFCs, from the Kuiper belt, and HTCs, from an as yet unclear source, with probable contributions from both the Oort cloud and the scattered disc of the Kuiper belt [31]. Damocloids (small bodies of unclear origin in cometary orbits, most likely having lost all the volatiles of the cometary nucleus) and asteroids in cometary orbits (ACOs) are inactive bodies with $T_J < 2$ and

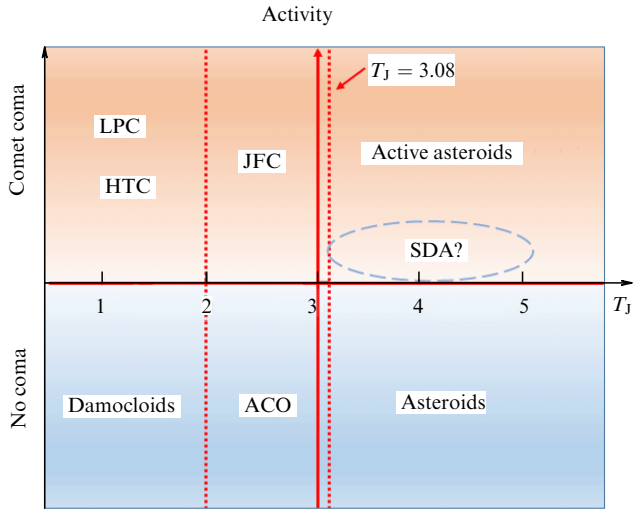

Figure 2. Classification of small bodies by dynamic parameter (Tisserand parameter T_J) and by signature of activity (coma detection). Abbreviations are explained in text. Vertical dotted line, designated $T_J = 3.08$, corresponds to nominal lower boundary for active asteroids. Region of asteroids with sublimation-driven dust activity (SDA) is shown conditionally. (Diagram adapted from [30].)

$2 \leqslant T_J \leqslant 3$, respectively. Centaurs (small bodies located between the orbits of Jupiter and Neptune, transitional in properties between MAB asteroids and Kuiper belt objects) are not shown in the diagram. They can be located anywhere in the diagram.

1.3 Asteroid activity: mechanisms

So, active asteroids are bodies that at least once have exhibited a detected pronounced sign of cometary activity (formation of a coma or tail). Such well-detected activity can arise under the effect of various mechanisms. Fairly comprehensive reviews of these mechanisms can be found in [22, 32, 33]. The main conclusion of these reviews is that sublimation is not the only mechanism driving the observed activity. Some bodies may not have ice at all, which particularly refers to silicate-rich asteroids known as S-type asteroids. Furthermore, the mechanisms potentially driving the observed activity are not mutually exclusive, and one mechanism of activity may trigger another or they may operate concurrently. Some events are stochastic (one-off) in nature, while others are repetitive. Repetitive activity is an important diagnostic indicator in determining the mechanism underlying the activity. We now briefly describe the main mechanisms of asteroid activity.

Sublimation of ice. The main mechanism of cometary activity is the sublimation of volatiles contained in the nuclei of comets in the form of ice. In addition to water ice, carbon dioxide and monoxide, ammonia, methane, nitrogen, and other molecules have been detected on asteroids and centaurs. Volatiles do not need to be on the surface to sublimate, but remote detection of ice on inactive bodies requires that the ice be present on the surface. Ice reservoirs in such bodies may be located either directly under the surface or deeper. Sublimation requires energy. Typically, this energy is provided by solar radiation. Many periodically active objects, especially comets, become more active as they approach the Sun. Energy may also come from other sources, such as tidal heating (for example, the heating of Europa, a satellite of Jupiter [30]) or phase transitions of ice (see [32]). The rate of sublimation of ice depends significantly on temperature. Any ice begins to sublimate more actively above a certain critical temperature, often called the sublimation temperature. The sublimation temperature may vary greatly for different types of ice. For example, study [35] reports theoretical values of the sublimation temperature of various types of ice at very low gas density (10^{13} cm^{-3}); for instance, for H_2O ice, the sublimation temperature is 152 K, while for CO it is 25 K. It is clear that water ice, for example, will not sublimate noticeably at typical orbital distances of centaurs, but it can easily sublimate on bodies in the asteroid belt. It can be expected that water ice can be preserved on a body orbiting at a radius of 5 AU, while such a body does not have reserves of carbon monoxide and methane due to their volatility [13, 36].

Impact events. Asteroid collisions are an ongoing process (especially in the MAB) that affects the formation of the size (mass) spectrum of asteroids and their orbital evolution. The collisional evolution of the asteroid population has been examined by many authors (see, for example, [37–39]). No direct observations of such events are available, and even observations of the implications of recent collisions are few. Registration of a recent collision is random observational luck. An example of such a lucky event is the object P/2010 A2. Immediately after its discovery on January 6, 2010 by the ground-based LINEAR telescope and observations by the Hubble telescope that followed soon after that, this unusual object was considered either a representative of the class of Main Belt comets or a manifestation of a collision of two asteroids of the Flora family. The second interpretation has been widely recognized [40]. It is believed that the first discovered active asteroid 4015 Wilson–Harrington (see Fig. 1) was impacted, since the activity of this object has never been observed again, despite searches that have continued for more than 70 years.

Asteroid 596 Scheila is considered an example of impact-induced asteroid activity [41]. Study [42] presents the results of observations of asteroid 596 Scheila and its ejecta cloud carried out using the ultraviolet optical telescope UVOT aboard the Swift spacecraft. None of the gases that are usually associated with increased volatility (CO^+, CO_2^+) or any volatiles emitted with dust (OH, NH, CN, C_2, C_3) have been detected. An estimated 6×10^8 kg of dust were ejected with a high ejection velocity of 57 m s^{-1}. According to [42], 596 Scheila most likely collided with another Main Belt asteroid with a diameter of less than 100 m.

Presented above are examples of the implications of collisions with fairly large bodies. However, much more frequently, asteroids collide with smaller bodies. In such collisions, some matter is ejected and/or the outermost layer of the target body is destroyed, i.e., its loosening (gardening) occurs. Loosening is a complex multifactorial process, which can be due to the action of micrometeoroids (impact gardening [43, 44]) and photons (loosening under the influence of radiation, solar gardening [45]). Impact gardening performs the important function of bringing ice closer to the surface of the body, thereby increasing the availability of material for sublimation.

Recently, the OSIRIS-REx spacecraft visited asteroid 101955 Bennu to collect samples. Cameras installed aboard the spacecraft recorded what looked like gravel and other solid particles flying off and returning to the surface (Fig. 3). Micrometeoroid impacts have been suggested as a potential

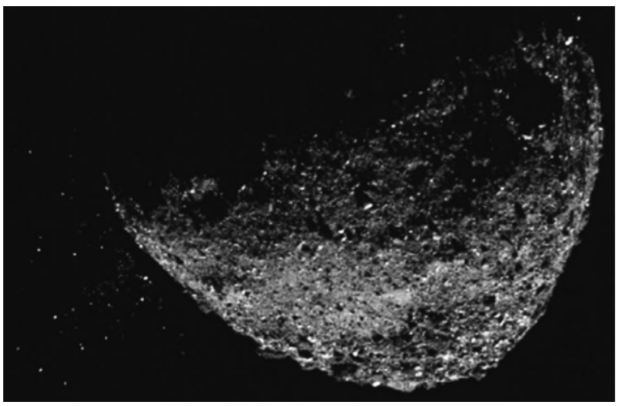

Figure 3. Gravel particles (left) ejected from the surface of asteroid 101955 Bennu were detected by cameras aboard the OSIRlS-REx spacecraft. (Source: NASA/Goddard/University of Arizona/Lockheed Martin.)

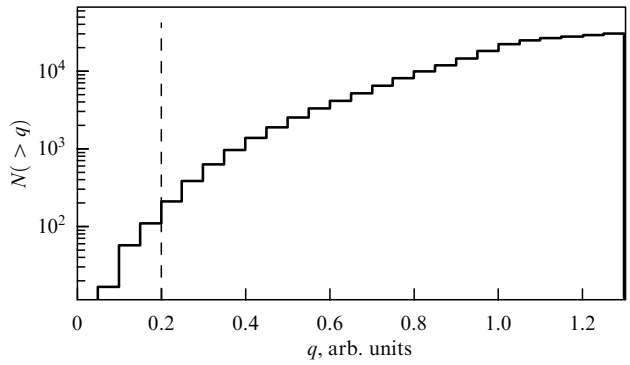

Figure 4. Distribution of NEAs by perihelion distance.

cause [46, 47], although an alternative mechanism, thermal disruption, is also discussed (see below in this section).

Rotational instability. Asteroids are subject to 'spin-up' over time through a process known as the Yarkovsky–O'Keefe–Radzievskii–Paddack (YORP) effect (for more on YORP, see, for example, [48]). It is plausible that rotational instability may lead to recurring activity unrelated to sublimation [22]. Even if activity does recur, its occurrence will not correlate with the distance to perihelion. Rotational instability may also lead to sublimation if, for example, a collapse or landslide exposes previously buried volatiles that subsequently sublimate. Activity may cease again if the volatiles are reabsorbed by the settling material that was previously ejected.

Thermal disruption. Heating solid materials can lead to their fracture. Fracture occurs when the stress caused by temperature change (e.g., expansion of heated material) exceeds the tensile strength of adjacent material. Depending on the orbit of the object, this can happen repeatedly, especially when the object is close to the Sun. This phenomenon alone can initiate ejection of material into space and comet-like activity. In addition, the formation of fractures can lead to the exposure of previously isolated ice, which subsequently sublimes.

Study [49] has shown that dynamic models of the population of near-Earth asteroids (NEAs) predict the number of bodies with perihelion distances close to the Sun larger than that provided by observations. It is suggested that NEAs with small perihelion distances undergo so-called supercatastrophic fracture due to a not entirely understood process. The mechanism of fracture, although clearly related to temperature, is not trivial. It is possible that rocks disintegrate into small fragments as a result of thermal cracking of the upper layer, and then the smallest particles are blown off the asteroid by radiation pressure. It is suggested in [50] that supercatastrophic destruction can also be due to collisions with meteoroids whose speeds and concentrations in the near-solar region are large. In this case, asteroids can throw off the upper layers repeatedly, although not periodically, and precisely in the perihelion zone, i.e., almost according to the cometary pattern. In general, such supercatastrophic destruction is relatively rare, since the number of NEAs with very small perihelion distances is relatively small. As can be seen from Fig. 4, plotted for an ensemble of known NEAs (data from the Minor Planet Center website[5]), the number of NEAs with $q < 0.2$ AU (thermal effects may be of importance only at high temperatures $T > 600$ K, which corresponds to $q < 0.2$ AU) accounts for only about 0.3% of the total.

In the case of the active asteroid 3200 Phaeton, which is believed to be responsible for the Geminid meteor shower (see, e.g., [51]), the body temperature reaches about 1100 K at perihelion (0.14 AU) [52], which can cause thermal destruction and, in turn, can lead to mass loss [53, 54]. The JAXA DESTINY + (Demonstration and Experiment of Space Technology for Interplanetary Voyage with Phaethon Flyby and Dust Science) mission, scheduled for launch in 2025, is designed to provide a more complete picture of Phaeton and its activity [55].

Radiation pressure on dust. Solar radiation pressure creates a force that could, in principle, sweep fine particles from the surface of an atmosphereless body, especially one with a weak gravitational field. This effect could play an important role as a secondary influence, carrying away material ejected due to other mechanisms (see below) that would otherwise settle back on the surface. This phenomenon is thought to be of importance in the case of asteroid 3200 Phaeton, given its $q = 0.14$ AU and the intense solar flux. To date, this effect has not been directly measured on the asteroid, but the DESTINY + mission may provide new data.

Electrostatic lift. This mechanism has been observed by Surveyor-5, 6, and 7 as 'lunar horizon glow' [56]. Electrostatic forces can be strong enough to push dust particles away from the surface of small atmosphereless bodies such as asteroids. If material is lifted with an energy insufficient to escape the body, a second mechanism (such as radiation pressure) may facilitate the carrying away of the material. Electrostatic lift is a weak mechanism, so it is unclear whether it could result in detectable activity at distances greater than the spacecraft's circumasteroid orbit [22].

Miscellaneous mechanisms. Other mechanisms of asteroid activity are also considered, including contact destruction in binary asteroids, dehydration of phyllosilicates, and even cryovolcanism (see, for example, [33]).

Cryovolcanism only occurs on large planetary satellites (for example, Enceladus [57]) or dwarf planets (Ceres [58]). It is currently unclear whether any activity on active asteroids or active centaurs is related to cryovolcanism.

Phyllosilicates are a class of mineral characterized by stratification, such as mica or smectite clays. Hydrated phyllosilicates contain volatiles such as water trapped

[5] URL: https://minorplanetcenter.net. Accessed June 1, 2023.

between the layers. Laboratory studies of meteorites rich in hydrated phyllosilicates show that volatiles can be released upon heating. This can lead to the ejection of material from the surface of an atmosphereless body. Such a mechanism may be operative on asteroid 101955 Bennu [46], since its surface is abundant in hydrated phyllosilicates [59]. However, it is assumed (see [46]) that three mechanisms for generating such emissions may be concurrently operative on the active asteroid 101955 Bennu: collisions of the asteroid with meteoroids, dehydration of phyllosilicates that are part of the asteroid's substance, and explosive destruction of rocks due to rapid heating and cooling. The last is possible due to too rapid a change between day and night on the asteroid.

The components of a binary asteroid may eventually converge into a contact binary system. Physical interactions between the contacting components of binary systems may result in the exfoliation of material from the surfaces, which leads to the formation of a coma and/or tail. However, this mechanism has yet to be definitively identified as the cause of activity of any known active asteroid, although it has been proposed as a possible explanation for the activity of asteroid P/2013 P5 [60].

1.4 Section conclusions

A comparative analysis of the above observations and asteroid activity mechanisms leads to the following conclusions:

(1) Asteroid activity has been detected primarily by imaging. In turn, spectral observations make it possible, in principle, to detect the activity of an object regardless of whether the substance consists of volatiles or dust. This method has also been used previously, but sublimation manifestations in Main Belt comets have not previously been confirmed in spectral observations from Earth's surface (see [36, 61]). Note that recent observations with the JWST space telescope have revealed water in the coma of the Main Belt comet 238P/Read [61].

(2) Ground-based observations reveal only sufficiently pronounced manifestations of activity that lead to the appearance of a coma and/or tail in a small number of asteroids. There is no doubt that the number of asteroids with activity on a more moderate scale is incomparably greater. New approaches are needed to detect weak activity with ground-based instruments.

(3) Many mechanisms can activate asteroids, but most of them are weak, and their manifestations can apparently only be detected via space missions.

(4) The most effective mechanisms are ice sublimation (for ice-containing bodies) and impact events (for bodies of any composition). These mechanisms are operative on bodies of all sizes.

(5) The impact mechanism is universal and can, through fragmentation, ensure the formation of small bodies ranging in size from fractions of a micron to asteroids, but it operates primarily in areas with a high concentration of impactor bodies (for example, in the Main Belt).

2. Sublimation-driven dust activity of asteroids

As noted in Section 1, novel approaches are needed to detect weak asteroid activity using ground-based instruments. The standard methods of broadband photometry and spectrophotometry prove to be effective approaches. In studies [1–4], the use of this approach enabled a large-scale exploration of the weak form of activity of primitive asteroids, called sublimation-driven dust activity (SDA). SDA leads to the formation of a temporary, fairly rarefied dusty exosphere around asteroids. This section presents spectral data that made it possible not only to detect SDA for a number of fairly large primitive asteroids of the Main Belt for the first time, but also to outline guidelines for their further research, including clarifying their origin and current composition of matter. Furthermore, numerical modeling of the reflectance spectra of such conditionally active asteroids and their comparison with observational data made it possible to specify the size, structure, and composition of matter of the dust particles that form their temporary dusty exosphere.

2.1 Evidence of active events on asteroids and detection of asteroid exosphere by spectral methods

One of the main features of asteroids as small celestial bodies has traditionally been the absence of not only a gas atmosphere but also a rarefied dusty exosphere (DE), since their gravitational field is very weak (weaker than Earth's by a factor of $\sim 30-10^5$) and cannot retain a DE for a long time, even in the largest asteroids. However, about three decades ago, several more very small objects, approximately a kilometer in size, were discovered in the MAB, which exhibited short-term comet-like activity. It can be assumed that it was due to emissions of dust and larger fragments associated with impact events or collisions of small asteroids. These results initiated an ongoing discussion about the possible activity of asteroids and their probable evolutionary connection with comet nuclei (see, for example, [20–22]).

The main mechanisms of asteroid activity have already been examined in a number of publications (see, for example, [22, 30]) and were also discussed above. We now explore in more detail the mechanism associated with the sublimation of H_2O ice from the surface layer of a primitive asteroid. It should be immediately emphasized that by such asteroids we mean primarily small bodies of taxonomic (spectral) types C, B, F, and G with low-temperature mineralogy. The analogs of their matter are considered to be carbonaceous chondrites of various chemical groups with characteristic manifestations of aqueous metamorphism.

Numerous observations and modeling of cometary nuclei show that differences in their activity depend on the degree of activity, phase state, and relative content of astrophysical ice included in their composition (see, for example, [62, 63]). Our observational results (see, for example, [1–4]) show that the sublimation activity of primitive asteroids resembles that of comets, but is significantly weaker and limited in time. At the same time, it is apparent that water ice should prevail among other volatile compounds in the composition of asteroids whose parent bodies were formed in the early solar system near the boundary of H_2O ice formation. Model calculations (see, for example, [63]) show that, at subsolar temperatures corresponding to heliocentric distances of MAB (~ 2.1–3.2 AU), the sublimation rate of water ice is almost seven orders of magnitude lower than that of carbon dioxide ice, whose physical parameters are close to those of water ice. This implies that, due to the high volatility of CO_2 ice, its presence in the depths of Main Belt asteroids is unlikely. Therefore, the sublimation and associated dust activity of primitive asteroids should be driven primarily by the content of H_2O ice. Moreover, the possibility of its preservation on the scale of the existence of the solar system in the depths of sufficiently

large primitive asteroids (a kilometer or more) is substantiated using numerical calculations [13].

Another important feature of the asteroids under consideration, which manifests itself with increasing size and mass, is the increase in the thickness of their regolith layer. This is known, for example, from the results of complex studies of the surface matter of Ceres [64], which contains a high proportion of fine dust. This arises from these bodies' predominant composition, notably microcrystalline water-bearing phyllosilicates (e.g., [65, 66]). During the sublimation of water ice (as one of the binding components of the regolith), submicron-sized particles can be carried away from the surface of active asteroids even by low-speed (about tenths of m s^{-1}) gas flows and result in the formation of a thin DE. However, at the same time, as is shown in Section 2.2, a DE consisting of submicron-sized particles can effectively influence the spectral characteristics of the discussed primitive asteroids in the near ultraviolet and visible ranges, which facilitates their detection by spectral methods. Thus, the sublimation activity of primitive asteroids can be more accurately defined by such a term as SDA. It is also natural to ask the question: can the spectral features of an SDA asteroid differ from its purely dust activity in the absence of ice particles in a DE or under the action of another activity mechanism? Section 2.2 presents numerical modeling of conditionally active asteroids' reflectance spectra, addressing this question.

It should be noted that the most common methods for detecting asteroid activity during ground-based observations are the analysis of their direct images and the study of their photometric profiles in photographs (usually in the V band) in comparison with point images of neighboring stars (see, for example, [63]). The appearance of any asymmetry in the image of an asteroid is interpreted as a sign of its activity in the form of a coma, tail, or ejection of matter associated with an impact event. The photometric method, in which monitoring the apparent stellar magnitude of the asteroid under study is accompanied by its calculation using standard formulas that link the known orbital and physical parameters of the asteroid, may be considered a variation of the direct method for detecting asteroid activity. In this case, a decrease in the observed apparent stellar magnitude of the asteroid compared to the calculated one is also interpreted as a manifestation of its activity.

A feature of our approach to studying active asteroids is the application of the spectral method, which has shown high efficiency in these studies, even with low spectral resolution. Moreover, low resolution is an advantage of spectrophotometry or the popular broadband photometric system UBVRI in detecting and studying the faintest astronomical objects. It was these methods that allowed us to be the first to obtain the results presented below.

It is also of importance to note that direct images of an active asteroid in the MAB obtained with large ground-based telescopes under good photometric conditions do not reveal any signs of its activity until the size of its coma or tail exceeds several hundred kilometers, which corresponds to hundredths of an arc second. At the same time, the spectral method allows detecting changes in the asteroid's reflectivity spectrum associated with the presence of a DE even at a smaller extent of the latter, i.e., below the spatial resolution limit. This is a probable explanation of the fact that the activity of many of the asteroids we have discovered has not yet been confirmed by direct observational methods [67].

Our observational programs aimed at detecting active objects primarily included asteroids of primitive types with orbital eccentricities of at least 0.1 (which undergo more significant changes in subsolar temperatures on the surface when moving from aphelion to perihelion). Another requirement was that the objects be located near perihelion, which corresponds to the highest surface temperatures. We now discuss the most important results of these studies.

Thus, low-resolution spectrophotometry ($R \sim 100$) and/or UBVRI photometry were the main methods of our observations, as a result of which, over a period of about a decade, reflectance spectra of ~ 300 primitive asteroids have been obtained. Reflectance spectra (or approximated reflectance spectra) of asteroids were calculated using spectra of nonvariable solar-type stars as analogues of the Sun, and nonvariable stars located in common CCD frames with asteroids were used to control photometric stability in UBVRI observations (see, for example, [65, 68]). Taxonomic classes and the main physical parameters of asteroids in which we discovered clear spectral signatures of SDA along with asteroids suspected of activity (for confirmation of which additional observations are needed) are presented in the table. The total number of the former is currently 16 (their names are highlighted in capital letters in the table), while the number of the latter is also 16. It is of interest that two asteroids with an enhanced geometric albedo value (> 0.10) were among the active ones. This is likely, since the presence of ice on such asteroids can be explained by their low-speed collisions with ice bodies.

In September 2012 [1], we first detected simultaneous activity in four primitive Main Belt asteroids (145 Adeona, 704 Interamnia) and two high-albedo asteroids (779 Nina, 1474 Beira) near perihelion using spectrophotometry. It should be kept in mind that the average composition of the surface matter of asteroids of various taxonomic (spectral) types was established by comparing their reflectance spectra, which characterize the chemical and mineralogical composition of the matter, with laboratory reflectance spectra of crushed meteorite samples, as their probable fragments (see, for example, [78–80]). However, the reflectance spectra of these four asteroids obtained in the range of ~ 0.36–0.95 μm (Fig. 5a–d) turned out to be completely different from their reflectance spectra from the SMASS II [6] database, which vary slightly in the visible range and are characteristic of bodies of silicate composition (see, for example, [81]).

Despite some differences in the composition of the surface matter of 145 Adeona, 704 Interamnia, and 779 Nina (according to the classification), their common spectral feature was an unusual maximum at 0.4–0.5 μm (Fig. 5a–c). We suggested in [1] that such similarity could be a sign of the activity of these asteroids and the presence in them of a DE, consisting of particles of similar sizes comparable to the wavelengths of the scattered light. At the same time, two unusual maxima were found in the reflectance spectrum of 1474 Beira, the larger of which was shifted to 0.65 μm (Fig. 5d). The measurement errors of the discussed normalized reflectance spectra of asteroids (here and below) are 1–2% in the center of the visible range and increase to 5–7% near its boundaries, and the spectra themselves are averaged characteristics obtained over a time interval of up to several hours. The indicated spectral features of active asteroids were analyzed using numerical modeling of light scattering

[6] URL: http://smass.mit.edu/data/smass/smass2/. Accessed July 14, 2024.

Table. Taxonomic (spectral) class and main physical parameters of asteroids.

Number and name	Diameter (effective), km	Class[a]	Geometric albedo	Rotation period[a], h	Phase angle[a], deg	Elongation angle[a], deg	e[a]	a[a]	Family[b]
19 Fortuna	200[a], 223.07[b]	G[1], Ch[2]	0.04[a], 0.05[b]	7.44	28.45–28.46	90.68–90.70	0.16	2.44	—
24 THEMIS	198[a], 202.25[b]	C[1], B[2]	0.07[a], 0.06[b]	8.37	19.45–21.36	91.22–111.20	0.12	3.15	Themis
51 Nemausa	136.16[a], 147.31[b]	CU[1], Ch[2]	0.10[a], 0.06[b]	7.78	9.23–11.26	150.72–156.29	0.07	2.37	—
52 Europa	303.92[a], 292.89[b]	CF[1], C[2]	0.06	5.63	9.04–9.05	153.79–153.80	0.11	3.09	Hygiea
65 CYBELE	237.26[a]	P[1], Xc[2]	0.07[a], 0.05[b]	6.08	9.12	145.21–145.22	0.12	3.43	Cybele
145 ADEONA	127.78[a], 150.95[b]	C[1], Ch[2]	0.06[a], 0.05[b]	15.07	10.14–25.81	55.03–154.20	0.15	2.67	Adeona
164 EVA	100.25[a], 73.03[b]	C[1], Ch[2]	0.06[a], 0.05[b]	15.07	10.14–25.81	55.03–154.20	0.15	2.67	Adeona
177 IRMA	69.05[a], 73.10[b]	C[1], Ch[2]	0.02[a], 0.04[b]	13.86	14.44–14.45	146.03–146.06	0.23	2.77	—
203 POMPEJA	124.59[a], 116.01[b]	DCX[1]	0.04	24.05	2.17	174.25–174.27	0.06	2.74	—
250 Bettina	121.00[a], 79.27[b]	M[1], Xk[2]	0.11[a], 0.23[b]	5.05	6.50–19.23	103.88–161.54	0.14	3.14	—
266 Aline	109.49[a], 108.84[b]	C[1], Ch[2]	0.03[a], 0.06[b]	13.02	10.46–10.48	153.27–153.32	0.15	2.81	—
302 CLARISSA	38.53[a], 42.99[b]	F[1]	0.05[a], 0.04[b]	14.38	117.22	139.45–139.46	0.11	2.41	Clarissa
322 PHAEO	69.86[a], 73.14[b]	X[1], X[2], D[2] [69]	0.09[a], 0.08[b]	17.58	7.22	162.54	0.24	2.78	Phaeo
360 CARLOVA	129.13[a], 115.62[b]	C[1], C[2]	0.04[a], 0.05[b]	6.18	17.43	116.13–116.14	0.17	3.01	—
379 Huenna	84.787[a], 87.34[b]	B[1], P[1] [70], C[2]	0.05[a], 0.06[b]	14.14	9.97–9.98	150.20–150.24	0.18	3.14	Themis
383 JANINA	43.48[a], 45.39[b]	B[1], B[2]	0.04[a], 0.08[b]	6.43	13.32–13.35	142.20–142.29	0.17	3.14	Themis
424 Gratia	102.57[a], 87.22[b]	X[1], [71], Xc[2] [71]	0.03	20.06	3.43–15.55	134.69–170.78	0.11	2.77	—
435 Ella	34.79[a], 41.34[b]	DCX[1]	0.12[a], 0.06[b]	4.63	11.51	153.04–153.05	0.15	2.45	Ella [72]
449 HAMBURGA	85.59[a], 87.16[b]	C[1]	0.04	36.52	24.58–27.79	99.34–117.99	0.17	2.55	—
629 Bernardina	35.09[a], 29.97[b]	X[2]	0.14[a], 0.18[b]	3.76	3.57–8.62	156.27–170.34	0.16	3.13	—
690 WRATISLAVIA	134.65[a], 134.42[b]	CPF[1], B[1] [71], B[2] [71]	0.06[a], 0.07[b]	8.64	8.56	155.24	0.18	3.15	—
704 INTERAMNIA	306.31[a], 316.46[b]	F[1], B[2]	0.08[a], 0.05[b]	8.73	13.68–22.69	86.55–142.36	0.16	3.06	Interamnia
750 OSKAR	22.53[a], 20.51[b]	F[1], C[1] [73]	0.06[a], 0.05[b]	6.26	13.20–13.21	148.88–148.90	0.13	2.44	Nysa-Polana
751 Faina	113.70[a], 110.18[b]	C[1], Ch[2]	0.03[a], 0.04[b]	23.68	14.80–17.10	132.82–138.27	0.15	2.55	Faina [74]
757 Portlandia	32.89	XF[1], F[1] [75], Xk[2]	0.22[a], 0.16[b]	6.58	17.10–19.50	131.63–138.64	0.11	2.37	Athor [76]
762 Pulcova	147.34[a], 136.88[b]	F[1], C[1] [71], Cb[2] [71]	0.04	5.84	11.15–16.51	125.75–145.87	0.11	3.15	—
778 Theobalda	55.32[a], 63.88[b]	F[1]	0.08[a], 0.05[b]	11.66	14.82–17.26	134.51–141.23	0.26	3.18	Theobalda
779 NINA	80.57[a], 77.45[b]	X[2], M [77]	0.16[a], 0.17[b]	11.19	8.55–26.23	114.64–157.15	0.23	2.66	—
859 Bouzaréah	65.42[a], 73.90[b]	C[1] [71], X[2] [71]	0.03[a], 0.04[b]	23.20	11.31–11.89	140.37–142.05	0.11	3.23	—
1121 Natascha	12.86[a], 12.41[b]	—	0.29[a], 0.27[b]	13.20	7.34–12.99	148.49–163.09	0.16	2.55	Astraea
1474 BEIRA	9.71[b]	FX[1], B[2]	0.20[b]	4.18	23.58–23.97	140.80–141.41	0.49	2.73	—
1687 Glarona	37.85[a], 33.66[b]	—	0.14[a], 0.08[b]	6.50	0.94–3.82	168.84–177.33	0.17	3.16	Themis

Note. Names are in capital letters for active asteroids (there are 16 of them) for which we have detected SDA and signs of DE. Objects for which only numbers are typed in bold feature an increased geometric albedo (> 0.10), which characterizes them as partially high-temperature bodies.
Legend. Source of information is indicated by superscript letters:
[a] https://ssd.jpl.nasa.gov/,
[b] https://www.minorplanet.info/,
[c] https://sbnarchive.psi.edu/ferret/.
Where data coincide, their source is not indicated. By default, values from JPL NASA website are taken as the main source. Classification is indicated by superscript numbers:
[1] according to Tholen classification (https://ssd.jpl.nasa.gov/);
[2] according to SMASSII classification (https://ssd.jpl.nasa.gov/).

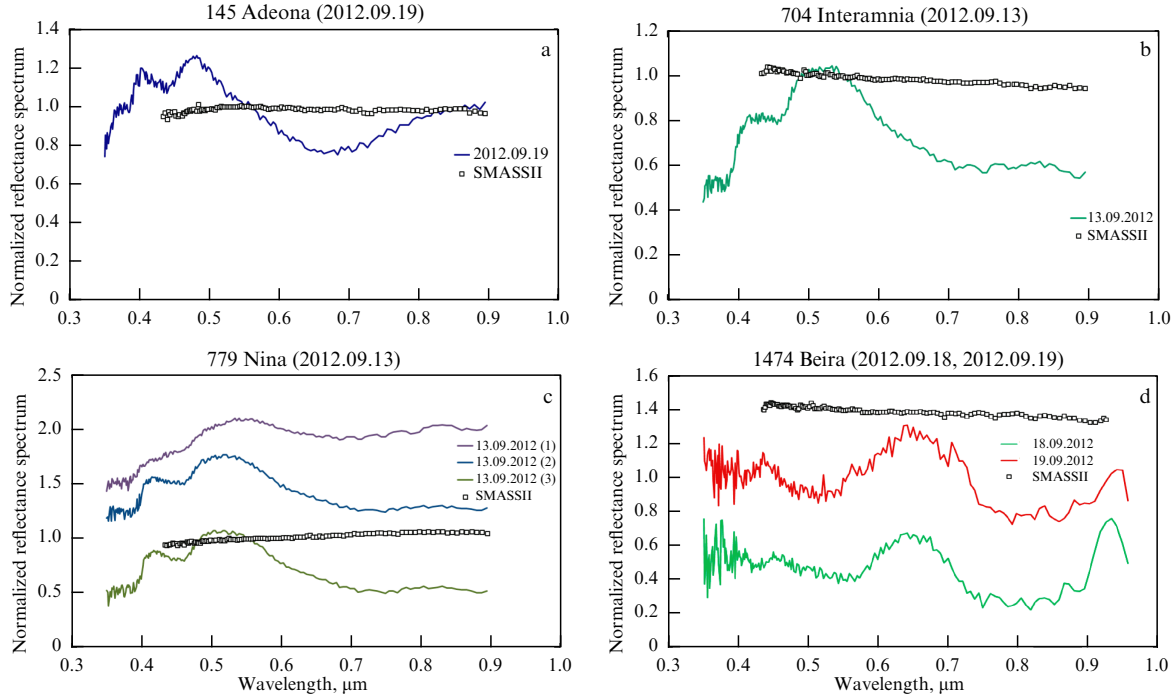

Figure 5. Normalized (here and below, at a wavelength of 0.55 μm) reflectance spectra obtained in September 2012 during active state of asteroids (a) 145 Adeona, (b) 704 Interamnia, (c) 779 Nina, (d) 1474 Beira (colored curves), and spectra of same asteroids previously measured in an inactive state (almost straight-line black curves from SMASS II database) [1].

in the dusty exosphere, the details of which are discussed in Section 2.2.

Recent astrometric and celestial mechanical studies have established that 145 Adeona leads one of the largest families of asteroids (6279 members) with similar orbital parameters [82, 83], which may also feature similar chemical and mineralogical properties, including subsurface water ice deposits.

It is necessary to pay attention to another important feature of SDA asteroids of primitive types — the phenomenon of their quasi-simultaneous activity (given the small difference in observation times). An explanation can be that these asteroids share some common properties that facilitate their transition to an active state under the influence of external factors. The main such factor may be the high subsolar temperature of their surface when passing near perihelion, since these asteroids were located at small perihelion distances during observations (except for Adeona, which was at that time at a distance of about 1 AU from perihelion) [1]. Given that primitive asteroids can be formed near or beyond the water ice condensation boundary, we suggested that the common property causing simultaneous SDA of asteroids is the presence of water ice in their composition in quantities sufficient to form a temporary DE. It is very likely that such a process begins on all asteroids in whose interiors water ice has been preserved, when surface ice outcrops caused by recent impact events occur. This hypothesis is supported by the data obtained using the InfraRed Astronomical Satellite (IRAS), showing the existence of at least three dust belts gravitationally bound to the MAB, which may be a sign of a high frequency of mutual collisions of bodies of various sizes (see, for example, [84]). Although the smallest particles (approximately one to several hundred microns in size) are relatively quickly removed from the MAB due to radiation pressure and the Poynting–Robertson effect [85], a sufficiently high concentration of fragmented and dust material is maintained there due to new cascade collisions [86]. This issue is discussed in more detail in Section 3.

In 2016–2019, during the subsequent perihelion passages of 145 Adeona, 704 Interamnia and 779 Nina, we again observed SDA of these asteroids by spectrophotometry and UBVRI photometry at different observatories. In 2016, SDA was first detected on asteroid 65 Cybele near perihelion; its spectral class is estimated as P or Xc [3]. Although only two reflectance spectra of Cybele near perihelion (Fig. 6) were obtained over a fairly short time interval (about 10 min), their significant changes under good photometric conditions compared to the spectrum of this asteroid from the SMASS II database indicate the presence of SDA. Although additional data are needed to draw more robust conclusions, Cybele's activity is confirmed by the results of observations in the near-IR range: diagnostic absorption bands of water ice and organic compounds appeared near 3 μm in its spectra, indicating surface ice.

Based on the results of the next series of UBVRI observations conducted in March and April 2019, we detected — for the first time — simultaneous SDA of asteroids 24 Themis and 449 Hamburga and — for the third time — of 704 Interamnia, when they were near perihelion [67]. The reflectance spectra of asteroids were used to detect, for the first time, solar-wind shock-wave passages likely caused by solar coronal mass ejections. Some differences in the heliocentric distances of the asteroids under discussion during their observations indicate that there was not one wave, but at least two successive waves with an interval of about a day. A more detailed discussion of the circumstances of these observations is continued in Section 2.3.

Based on the UBVRI data on 24 Themis, 449 Hamburga, and 704 Interamnia, we calculated their reflectance values at the effective wavelengths of the photometric bands (0.36, 0.44, 0.55, 0.64, and 0.80 μm), and then their approximated

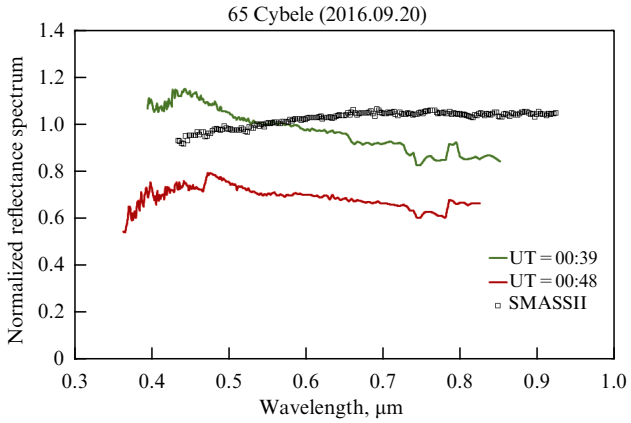

Figure 6. Normalized reflectance spectra of 65 Cybele in an active state, obtained in 2016 with a time interval of about 10 minutes (colored lines). Sharp change in shape of asteroid's reflectance spectrum can be explained by scattering of reflected light from the asteroid in an irregular DE consisting primarily of submicron-sized water-ice particles (see Section 2.2). For comparison, normalized reflectance spectrum of this asteroid without signs of activity from SMASS II database is shown.

reflectance spectra were constructed (in the form of broken curves shown in different colors) in a range of 0.36–0.80 μm (Fig. 7a–c) [67]. The absence of data in the U band on March 17 and 19 and April 10 in the presented characteristics of asteroids is due to the high background level in this band and the low signal level. The double-peaked or single-peaked (April 10, 2019) shapes of the approximate spectra of the observed asteroids, similar to the shape of the spectra of four active asteroids in September 2012, do not reflect surface composition but indicate a DE. This conclusion is also confirmed by the coincidence of the presented approximated reflectance spectra of 24 Themis and 449 Hamburga with similar characteristics of 704 Interamnia, which was observed together with them; the activity of 704 Interamnia at perihelion was discovered and confirmed earlier [1, 3].

On March 18, 2019, we observed the simultaneous disappearance of the **double-peaked** spectral shapes for 24 Themis, 449 Hamburga, and 704 Interamnia, **indicating** a DE. The shape of the spectra changed to the usual one, characteristic of the solid surface of asteroids (which was also confirmed by the coincidence of the spectra observed on March 18 with the 'canonical' spectra from the SMASS II database (Fig. 7a–c)). However, the shape of the reflectance spectra, indicating the activity of asteroids, was restored on March 19, 2019. This event can be explained by the removal of the DE from the subsolar side of the asteroids in question by shock waves in the solar wind close in time, which reached them immediately before the observations on March 18. Considering slight differences in heliocentric distances (Themis, Interamnia, and Hamburga), we infer **multiple** shock-wave passages. We return to a more detailed analysis of this event in Section 2.3.

We now briefly discuss other important information about 24 Themis. Using ground-based IR observations near the absorption band at about 3 μm, water ice and organic compounds were discovered on the surface of Themis, and it was shown that they are predominant on the surface [23, 88]. According to data from AKARI, a Japanese IR satellite, the presence of hydrated minerals was revealed on Themis [89]. Another publication on 24 Themis and 1 Ceres presents estimated rates of sublimation of water ice based on the emission line [O I] 6300 Å, which are, respectively, (as upper limits) 4.5×10^{27} and 4.6×10^{28} molecules per second [90]. Although Themis is one fifth the size of Ceres, the emission of gaseous H_2O during ice sublimation from the surface of these bodies turned out to be comparable. The approximate estimates given correspond to a very small part of the active surface of the asteroids under discussion (less than 2×10^{-4}), but the authors admit that this relative value may vary by an order of magnitude, depending on the heat-conducting properties of the surface. It is also emphasized that cometary nuclei have significantly larger active regions ranging from tenths to hundredths of the surface area [90].

It should be noted that 24 Themis, like 145 Adeona, leads one of the largest families of asteroids (12,288 members) [82, 83], which may have similar chemical and mineralogical properties, given their supposed common origin. It was proposed (see, for example, [91]) to carry out ground and space studies of 24 Themis, which probably is the ice core of some parent body from which its entire family could have formed. If this is indeed the case, most of the asteroids that are part of the Themis family have a rock-ice composition. However, despite the signs of significant deposits of water ice in the depths of Themis itself, this cannot be attributed with certainty to other members of this family, especially small ones, if the hypothesis of their common impact origin is true.

In December 2020, we carried out spectrophotometric observations of six primitive-type Main Belt asteroids: 19 Fortuna, 52 Europa, 177 Irma, 203 Pompeja, 379 Huenna, and 383 Janina (see the table), which feature significant orbital eccentricities and were located near perihelion distances [92]. The aim of these studies was to determine the influence on the asteroid reflectance spectra of not only maximum subsolar temperatures but also recent solar activity events. According to data obtained from the GOES-16 and SOHO satellites, during a period of general low solar activity that determines a fairly quiescent state of the interplanetary medium, the listed asteroids approximately 10 days before the start of our observations were affected by a significant M–X class solar flare in the X-ray range and the associated coronal mass ejection (CME) near the equatorial plane of the Sun at the end of November 2020.

To detect signs of activity of the aforementioned asteroids, we compared their normalized reflectance spectra in a range of $\sim$ 0.36–0.95 μm with so-called templates (two-dimensional r–λ regions plotted on the field of dependence of the relative reflectivity of the asteroid r on the wavelength λ for all possible variations in the normalized reflectance spectra of asteroids of the corresponding spectral types in an inactive state according to databases [78] and [79]). In the plots with the reflectance spectra of the asteroids displayed in Fig. 8a–f, such regions are colored light green. Significant, sometimes abrupt deviations appeared beyond the template boundaries (for example, for 19 Fortuna, Fig. 8a) in the absence of noticeable changes in the spectral transparency of Earth's atmosphere during these observations [92]. Such features can be interpreted as manifestations of a mobile but irregular DE or even as the formation of separate dust ejections in asteroids under the effect of waves in the solar wind. It is possible that the activity of these asteroids was not strong enough to form a more stable temporary DE with spectral features in the form of the mentioned one or two maxima in the visible range. A spectral feature similar to SDA, but comparatively weak, was detected only in the short-

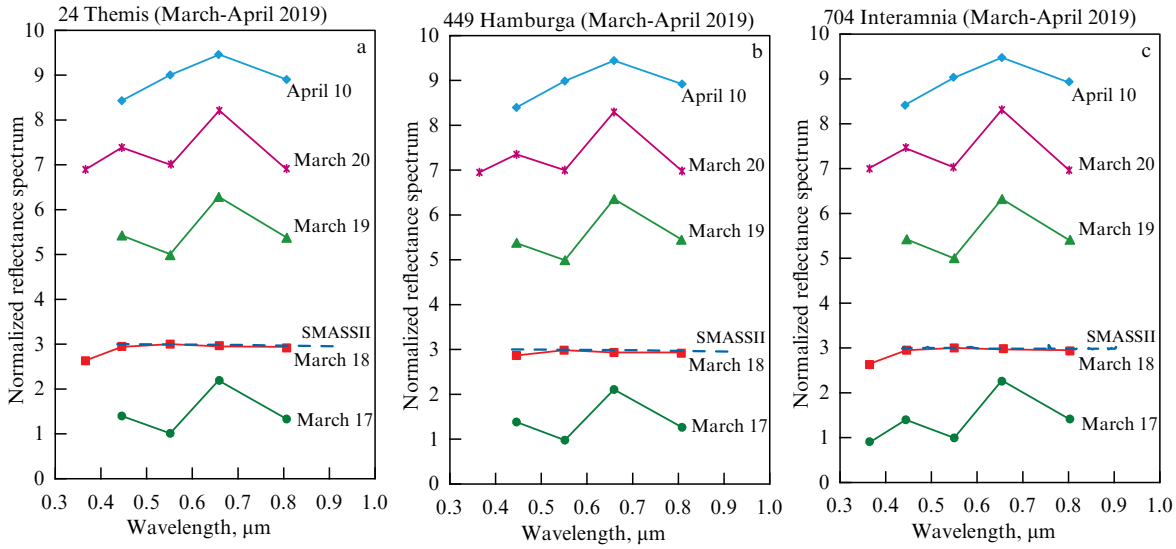

Figure 7. Normalized approximated reflectance spectra of (a) 24 Themis, (b) 449 Hamburga, and (c) 704 Interamnia obtained from UBVRI photometric data for March 17–20 and April 10, 2019, when the asteroids were active and very close to perihelion [67]. Spectra are normalized to value at 0.55 μm and arbitrarily shifted along vertical axis for ease of comparison. Reflectance spectra measured on March 18 correspond to surfaces of these asteroids and follow their 'canonical' reflectance spectra from SMASS II database.

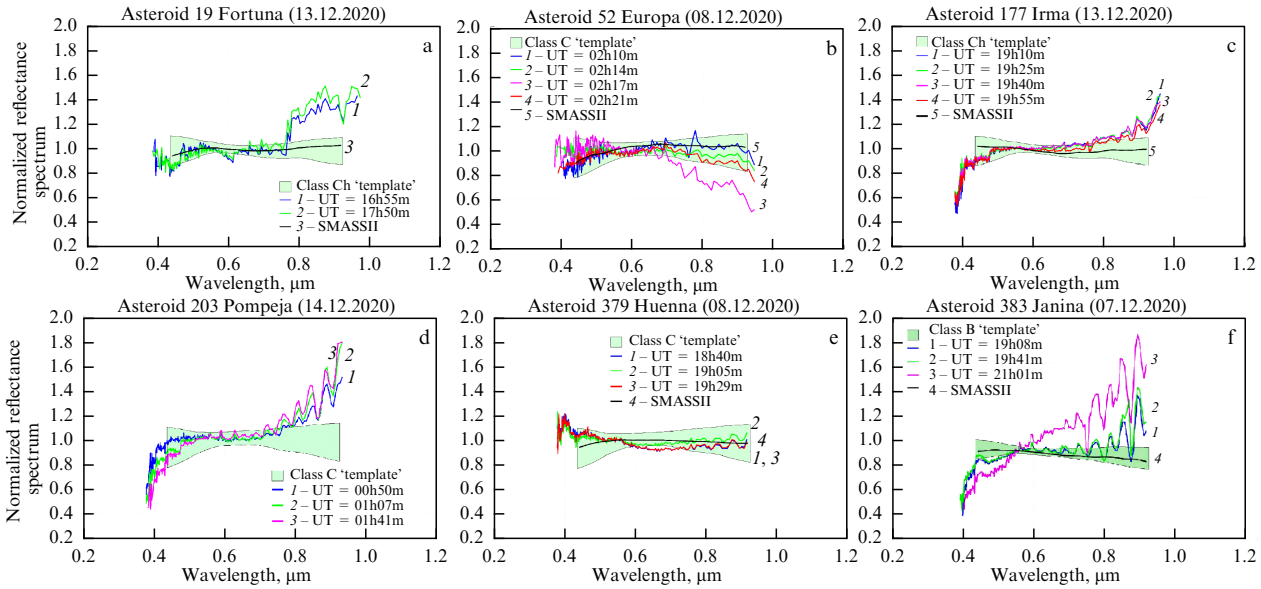

Figure 8. Normalized reflectance spectra of active asteroids (a) 19 Fortuna, (b) 52 Europa, (c) 177 Irma, (d) 203 Pompeja, (e) 379 Huenna, and (f) 383 Janina, obtained sequentially on December 7–14, 2020. 'Templates' of their taxonomic types are shown by light green areas. Several sequential multi-colored reflectance spectra of each asteroid are shown against 'templates' background, and their 'canonical' normalized reflectance spectra without signs of activity from SMASS II database are shown by thick black line; reflectance spectrum of asteroid 203 Pompeja is not available in this database.

wave part of the reflectance spectrum of 379 Huenna (Fig. 8e). At the same time, unusual regular 'comb-shaped' structures were detected in the reflectance spectra of 177 Irma, 203 Pompeja, and 383 Janina. They are discussed in Section 2.3, devoted to the influence of the above solar events on active asteroids.

From December 2021 to February 2022, and from December 2022 to March 2023, we conducted two UBVRI surveys of Main Belt asteroids accessible for observation at the Caucasus Mountain Observatory (CMO) of the Sternberg Astronomical Institute of Moscow State University. The 0.6-m semi-automatic RC600 telescope was used to search for active objects among these asteroids applying a unified technique. The observations included asteroids of primarily primitive types located near perihelion distances [68, 93]. The first of these surveys provided data on 29 asteroids, and the second, on 65. Along with the asteroids, we observed nonvariable solar-type stars (with a minimal difference in coordinates) for the subsequent calculation of approximated reflectance spectra of asteroids in a range of 0.36–0.80 μm at effective wavelengths of five photometric bands. It should be noted that the number of G-type stars used included only those whose U–B color index was close enough to that of the Sun. As shown below using modeling of the reflectance spectra of an imaginary active C-type asteroid (in Section 2.2), the accuracy of measuring the slope of the reflectance

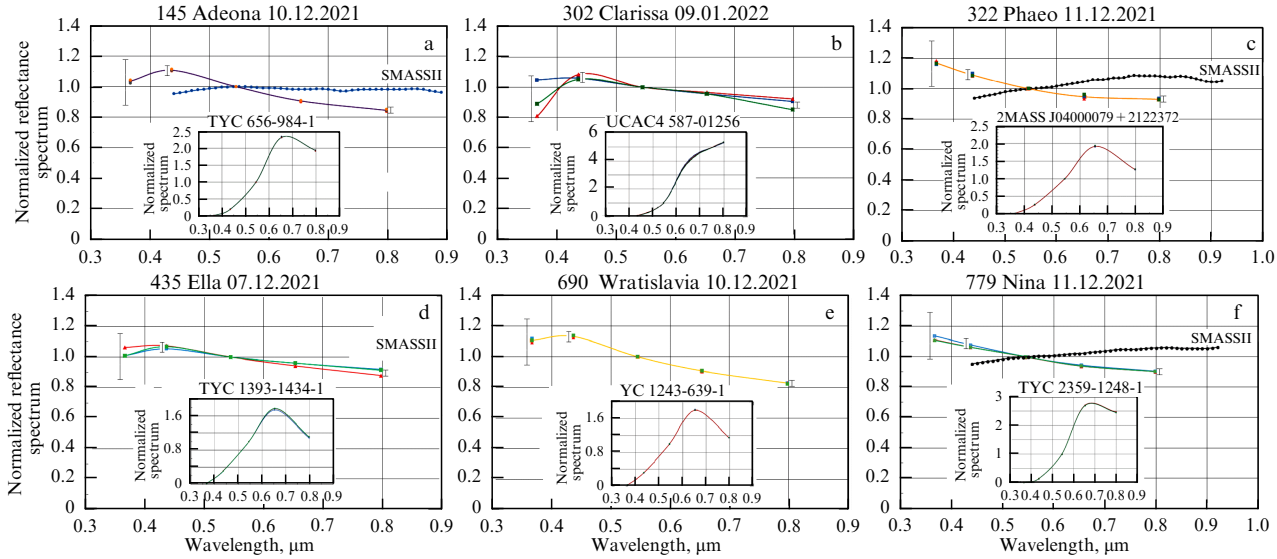

Figure 9. Normalized approximated reflectance spectra of asteroids with SDA features: (a) 145 Adeona, (b) 302 Clarissa, (c) 322 Phaeo, (d) 435 Ella, (e) 690 Wratislavia, and (f) 779 Nina. Plots of 145 Adeona, 322 Phaeo, and 779 Nina show normalized reflectance spectra of these asteroids from SMASS II database for comparison. Plot insets show spectra of nonvariable stars observed concurrently with the asteroids. Measurement error limits (obtained when calculating FWHM of UBVRI bands) are presented for U, B, and I photometric bands. For V and R bands, they were less than 1% and are therefore not shown.

spectrum of the observed asteroid in the short-wave part of the range is critically important for identifying signs of activity in it.

Another methodologically novel solution for obtaining observational data on active asteroids, along with the use of broadband UBVRI photometry, was the use in our analysis of nonvariable control stars, located on the same CCD frames as the asteroids, to monitor the spectral stability of the extinction of the atmosphere at the moments of their observations. By calculating and comparing successive approximated spectra of asteroids and control stars (see the insets with the spectra of stars in the plots in Fig. 9), such monitoring can be carried out at the qualitative and quantitative levels. By qualitative-level coincidence, three such consecutive spectra of the control star show that atmospheric variations are negligible over the entire range. At the same time, several consecutive (serial) reflectance spectra of active asteroids differ significantly, especially in the short-wave part of the spectra.

The main result of the 2021–2022 survey is the detection of significant spectral features of quasi-simultaneous SDA of six primitive-type Main Belt asteroids: 145 Adeona, 302 Clarissa, 322 Phaeo, 435 Ella, 690 Wratislavia, and 779 Nina (for the first time in 302 Clarissa, 322 Phaeo, 435 Ella, and 690 Wratislavia), which amounted to $\sim 24\%$ of the total number of bodies included in this observational program. The reflectance spectra of the listed asteroids are displayed in Fig. 9 as examples. Possible spectral manifestations of activity with lower intensity were first detected in five more asteroids (424 Gratia, 751 Faina, 762 Pulcova, 778 Theobalda, and 859 Bouzaréah), to be classified as suspected of activity (see the table). It is important to note that sublimation-driven dust activity of 145 Adeona and 779 Nina near perihelion was detected by us for the third time over the past decade, which corresponds to approximately three periods of their revolution around the Sun. However, the problem of the duration of SDA near the perihelion of the asteroids under discussion (as well as 704 Interamnia, whose SDA has already been confirmed several times) remains poorly understood. This will certainly be included in the list of tasks for our further research.

Although the 2022–2023 UBVRI survey observations included approximately twice as many MAB objects as the previous survey, their main result was the detection of SDA signatures in only three low-albedo asteroids (Fig. 10): 164 Eva, 360 Carlova, and 750 Oskar; in four more asteroids — 629 Bernardina, 757 Portlandia, 1121 Natascha, and 1687 Glarona — such signatures are unclear and are probably due to an alternative mechanism. However, in these observations, we were able to obtain additional important information [93]. Compared to the previous survey, the observed MAB asteroids included significantly more bodies with combined spectral types and smaller bodies (with the smallest effective diameters of up to ~ 8 km), which can be assumed to be a consequence of their more significant impact processing over the entire period of their existence. The two mentioned observations, taken together or separately, can be considered to be evidence that the conditions in the interiors of such asteroids may be more unfavorable for the survival of water ice on a cosmogonic time scale and, consequently, for the potential possibility of its sublimation at the present time.

To interpret the measured reflectance spectra of active asteroids, light scattering in the exosphere of a conventional asteroid was numerically simulated. The results of the calculations are presented in Section 2.2; it is also shown that measurements in the near and middle UV range are most promising for identifying the SDA of primitive asteroids and water ice as its main source.

Another important issue is the mechanism of variations in the reflectance spectra of active asteroids with rarefied and mobile DEs. In those regions of the spectral range used in observations where scattering by exospheric particles of various sizes or compositions leads to a different behavior of the spectrum, more frequent spectral oscillations are possible

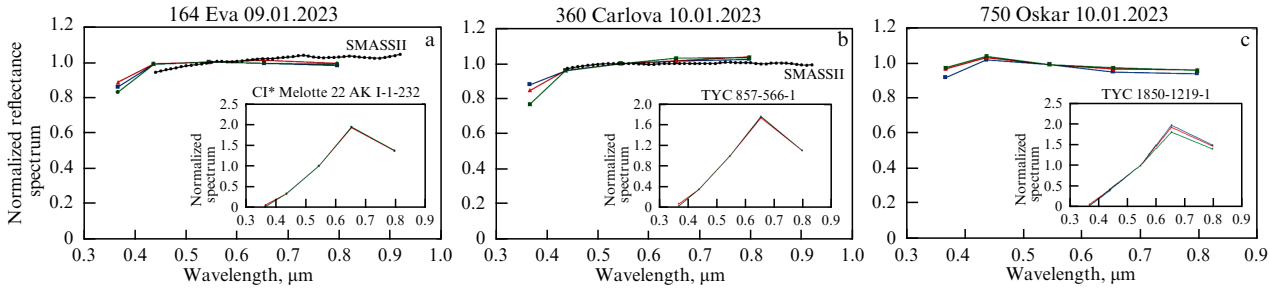

Figure 10. Normalized approximated reflectance spectra of asteroids with SDA signatures: (a) 164 Eva, (b) 360 Carlova, and (c) 750 Oskar compared to normalized spectra of nonvariable control stars (in insets) observed concurrently with the asteroids. Reflectance spectra of 164 Eva and 360 Carlova are also compared with their 'canonical' reflectance spectra from SMASS II database.

in the mobile DE under the influence of high-frequency oscillations in the solar wind. Affected by a significant electrostatic field of a photoemission nature on the subsolar side of the asteroid (see, for example, [94]), the smallest dust particles, regardless of the mechanism of their ejection from the surface, acquire an electric charge ([93] and references therein) and are subject to the influence of frequent and irregular density waves in the solar wind [95–97]. On the other hand, in primitive-type asteroids, the DE itself can be inhomogeneous, since it is usually formed from a gas-dust flow emerging from a local outcrop of water ice that occurs during a meteoroid impact. At the same time, the axial rotation of an active asteroid should gradually lead to a more uniform distribution of the DE over its surface, especially in the absence of significant shock waves in the solar wind.

Thus, a more detailed study of the obtained reflectance spectra of primitive active asteroids with weak manifestations of activity led us to the conclusion that a special quantitative criterion should be developed that would make it possible (with its certain values) to more reasonably assert precisely the SDA of a specific asteroid, and not an alternative mechanism of its dust activity. At the qualitative level, it is clear that such a criterion can be based on the information about the magnitude of spectral variations in the reflectance spectra of active asteroids in narrower spectral regions of the working range, where, according to numerical modeling, the spectral characteristics of ice and other DE particles differ most significantly, which leads to the greatest amplitude of short-period variations in the intensity of the recorded light flux. Based on this idea, we compared the root-mean-square errors in the intensity of the luminous flux recorded in the U band from the active asteroid $\Delta I_{\text{ast.}}$ and the nonvariable control star $\Delta I_{\text{control star}}$, and came to a conclusion about the weak SDA of the asteroids 164 Eva, 360 Carlova, and 750 Oskar (based on the positive value of the indicated difference and a signal-to-noise ratio of the asteroid of at least several dozen) [98].

2.2 Numerical modeling of light scattering in dusty exosphere and properties of its particles

2.2.1 Introductory remarks. To understand how the exosphere formed around an asteroid can change its reflectance spectrum, it is necessary to determine how the scattering characteristics of exospheric particles — the phase function (indicatrix), the albedo of single scattering, and the scattering efficiency — behave depending on the wavelength. Calculations of these characteristics are based on the assumption that dust particles in the exosphere are similar to those found in interplanetary space and in the comas and tails of comets (see, for example, [99–102]). Among them there are both densely packed solid particles with sizes of tenths and hundredths of a micron, and larger particles of an aggregate structure consisting of submicron grains, the sizes of which are somewhat smaller than or comparable to the wavelength of visible light. The complex morphology of cometary dust particles is also indicated by the results of an analysis of polarimetry of comets, according to which the grain size parameter in aggregate particles of cometary dust $x \equiv 2\pi r/\lambda$ (where r is the radius of the constituent grains and λ is the wavelength) is approximately in a range from 1.0 to 2.0 (see, for example, [103–107] and references therein). With such a relationship between the wavelength of light and the sizes of scatterers, the enhancement of collective effects in the scattering by ensembles of particles significantly affects the intensity and polarization of light scattered by the aggregate. As a result, the behavior of the specified characteristics for particles of a complex structure and homogeneous particles of the same sizes and composition differs noticeably. This, in turn, necessitates taking into account the aggregate structure of scattering particles in model calculations when interpreting measurements (see, for example, [105, 108–112] and references therein).

Results of studying the scattering characteristics of homogeneous particles depending on the wavelength, size, and refractive index are widely reported in publications (see, for example, [113, 114]). In particular, it is of importance that, if the size parameter is less than ~ 3, the intensity of light scattered by such particles increases significantly with decreasing wavelength (if the absorption coefficient of the substance is spectrally neutral), and the scattering characteristics of irregularly shaped particles can be calculated in the Lorentz–Mie approximation for spherical particles.

In what regards the scattering characteristics of aggregate particles, data on their spectral dependence are much scarcer. They mainly refer to either the IR range or integral characteristics — scattering and extinction cross sections (see, for example, [115]). At the same time, the angular dependence of the scattered light intensity is known to be also sensitive to the morphology of the scattering particles (see references above). The manifestation of collective effects in the intensity spectrum of visible light back-scattered by aggregate structures consisting of submicron grains was recently investigated in [116]. It was shown that interference features are formed in such a spectrum due to both scattering by individual constituents of the aggregate and scattering by their groups.

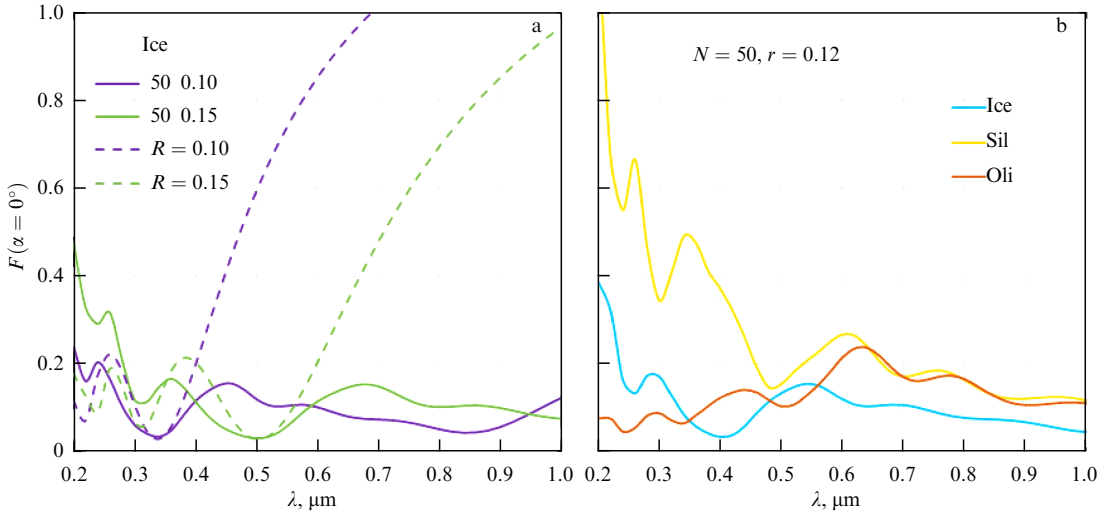

Figure 11. Spectral dependences of $F(\alpha = 0^\circ)$ for aggregate particles of H_2O ice consisting of 50 monomers with a radius of 0.10 and 0.15 μm and single particles of indicated radii R (a) and for aggregate particles consisting of 50 monomers with a radius of 0.12 μm of indicated composition (ice 'Ice', silicates 'Sil', and olivine 'Oli' (b). (See details in Section 2.2.2.)

Since this result is of importance for interpreting the reflecance spectra of active asteroids with an exosphere, we explain it in more detail. Recall that the intensity of radiation scattered by a particle depends on the value of the phase function F at a given phase angle α and on the scattering cross section of the particle C_{sca}. Calculations show that, for particles with a complex structure, the spectral dependence of C_{sca} turns out to be generally similar to the spectral dependence of C_{sca} of homogeneous particles of approximately the same mass, only shifted to the region of short wavelengths [117]. As for the spectral dependence of the phase function of aggregate particles, in our case, it is reasonable to consider the spectrum of F at a phase angle $\alpha = 0^\circ$, since the intensity of radiation scattered into the back hemisphere is important for interpreting the results of ground-based observations.

The spectra of $F(\alpha = 0^\circ)$ calculated for ice aggregate particles consisting of monomers with a radius of 0.10 and 0.15 μm, and aggregate particles of various compositions consisting of monomers with a radius of 0.12 μm, are presented in Fig. 11a and 11b. The details of the calculations and the data on the refractive index of the substances under consideration are given below in Section 2.2.2. Figure 11a also displays the spectral dependences of $F(\alpha = 0^\circ)$ for single spherical particles with a radius of $R = 0.10$ and 0.15 μm. It is apparent that the positions of the minima of the curves in the short-wavelength part of the spectrum for single particles and aggregates consisting of the same particles coincide, whereas at longer wavelengths additional details appear in the spectrum of aggregates. As shown in [116], at short wavelengths, the extrema of the phase function of aggregates of submicron constituents are due to the interference of electromagnetic waves scattered by individual monomers of the aggregate, while the details at longer wavelengths are due to the interference of waves scattered by groups of monomers.

The formation of the interference pattern in the $F(\alpha = 0^\circ)$ spectrum of individual submicron particles can be explained, and the position of the extrema can be roughly estimated using the geometric optics approximation (in this case, it provides a reasonable estimate, although for particles small compared to the wavelength it cannot be correct in general). The observed extrema are the result of the interference of waves, one of which, when incident on a particle of radius R with a complex refractive index $m_r + im_i$, is reflected from its outer surface, while the other passes through the particle twice and returns. Then the phase difference of these waves is $\delta = 4Rm_r$, and the position of the interference minima in the spectrum of radiation scattered by a single particle can be estimated as $\lambda_n = \delta/(n + 0.5)$, where n is an integer. For H_2O ice particles, we obtain $\lambda_1 \approx 0.34$ and 0.50 μm for $R = 0.10$ and 0.15 μm, which agrees with the plot in Fig. 11a. At higher m_r values, the agreement with the formula for λ_n becomes worse, and if absorption is significant, this approach yields incorrect estimates.

The main interference minimum (at λ_1) in the $F(\alpha = 0^\circ)$ spectrum, caused by scattering on individual monomers in the aggregate, shifts to longer wavelengths with an increase in the monomer size (Fig. 11a). The same effect is observed with an increase in the real part of the refractive index of the particles. From Fig. 11b, it is evident that, with an increase in m_r (for example, when passing from ice to olivines), λ_1 shifts from ~ 0.40 to ~ 0.52 μm (with a monomer radius of 0.12 μm). In the $F(\alpha = 0^\circ)$ spectrum for aggregates, immediately after the main minimum, a so-called 'collective' maximum is formed, which is due to the interference of waves scattered by groups of monomers. Calculations show that, with a sufficiently large number of monomers in the aggregate, the position of this maximum becomes independent of the number of monomers and the structure of the aggregate, and shifts slightly if the aggregate grains have sizes that differ from the average within 20% [116, 117].

Thus, the position of the main maxima and minima that set the general shape of the $F(\alpha = 0^\circ)$ spectrum depends primarily not on the size of the aggregates themselves but on the sizes of their grains and the composition of the substance. This allows us to limit modeling to relatively small structures, although, naturally, in real exospheres, the particles can be larger or smaller than those considered here. Therefore, it is necessary to remember that the reflectance spectra of active asteroids with an exosphere containing aggregate particles presented below are based not on the characteristics of the particles themselves but on their scattering characteristics.

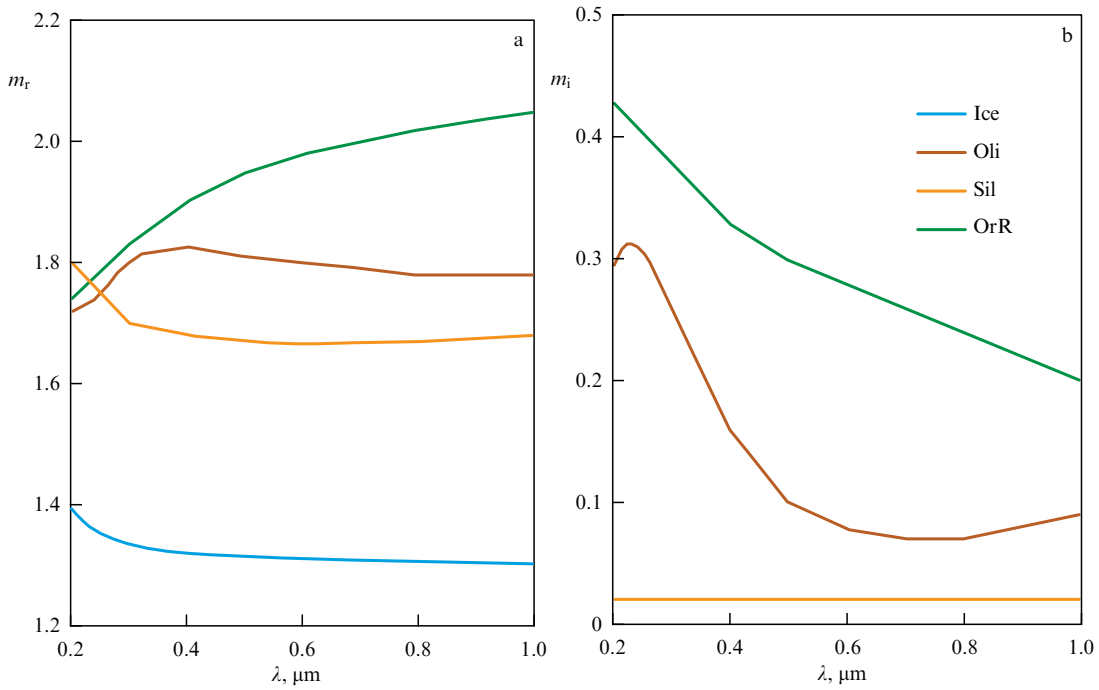

Figure 12. Spectral dependences of (a) real m_r and (b) imaginary m_i parts of refractive index of substances under consideration. For H_2O ice, m_i values are close to zero in this spectral range (see references in text).

2.2.2 Input parameters and procedure to calculate the reflectance spectrum of an active asteroid. The calculations of the reflectance spectrum of an active asteroid with a dust exosphere, the results of which are presented below in this section, assumed that the exosphere consists of either homogeneous submicron spherical particles or aggregates thereof.

The elements of the single scattering matrix and the scattering and extinction cross sections of homogeneous particles were calculated in the Lorenz–Mie approximation (see, for example, [114]) for a power-law particle size distribution for several values of the effective radius and the effective variance: $R_{\text{eff}} = 0.1-0.2$ μm and $v_{\text{eff}} = 0.02-0.1$.

A detailed description of the aggregate particles for which the calculations were made is presented in [117]. In generating these particles, we proceeded from the concept of a statistically fractal structure of cometary dust agglomerates (see, for example, [118]) and formed fractal-like aggregates (clusters) of identical spherical submicron grains (monomers) using the process of diffusely limited aggregation [119]. Several variants of structures with different porosities (from 0.54 to 0.90) consisting of 50 and 100 monomers were formed. Four values of the monomer radius $r = 0.08$, 0.10, 0.12, and 0.15 μm were chosen for the calculations. The characteristics of scattering on such complex morphology particles were calculated using the numerically exact T-matrix superposition method [120, 121].

Since the refractive indices in the range under consideration of some of the substances that can be expected to be present in the exospheric particles feature similar values and spectral behavior, this modeling was limited to four variants: H_2O ice ([122]; designated below in the figures as 'Ice'), olivines ([123]; 'Oli'), astronomical silicates ([124]; 'Sil'), and refractory organics ([124]; 'OrR'). The spectral dependences of the real m_r and imaginary m_i parts of the refractive index of the substances under consideration are presented in Fig. 12.

The elements of the single scattering matrix and the scattering and extinction cross sections calculated for exospheric particles were used as input parameters in the procedure for calculating the radiative transfer in the exosphere above the asteroid surface (for the method of invariant embedding used in calculations, see [125]). The optical thickness of the exosphere adopted in the model calculations varied from $\tau = 0.1$ to 6.0 at $\lambda = 0.55$ μm, while the values of τ along the spectrum were calculated based on the variation in the scattering cross section of model particles with the wavelength.

In what regards the gas component of the exosphere, its influence on the reflectance spectra of asteroids with an exosphere was not taken into account in most cases, since it is small and can manifest itself as a small smooth increase in brightness in the short-wavelength range [67]. This approximation is consistent with the estimates in [126], according to which the contribution of gas to the optical thickness of the coma of comet 67P/Churyumov–Gerasimenko at perihelion is very small.

To calculate the intensity of light scattered by an optically thin medium with an underlying surface, it is necessary to specify the reflection law for this surface. Since asteroids are usually observed at phase angles significantly greater than zero, it is possible to ignore the opposition effect (a significant increase in brightness characteristic of regolith surfaces when approaching opposition) and assume that the asteroid surface scatters light isotropically, which makes the calculation procedure much simpler and faster.

In calculating the model spectra presented below, a surface albedo value of $A_s = 0.072$ on $\lambda = 0.55$ μm, typical of low-albedo Main Belt asteroids (see, for example, [3, 127]), was adopted. The surface spectrum adopted in this modeling is shown in Figs 13–17 by the additional curve. At wavelengths $\lambda > 0.35$ μm, it follows the canonical

dependence for the C-type asteroid 145 Adeone retrieved from the SMAS-SII[7] database, which corresponds to the 'inactive' state of the asteroid, since it was obtained approximately six months before its perihelion passage. The expected decrease in A_s in the short-wavelength range expected for low-albedo asteroids, where SMASS II data are not available, was set based on the results of studies [128].

2.2.3 Model reflectance spectra of an asteroid with an exosphere. This section presents examples of reflectance spectra $B_{\rm norm}(\lambda)$ calculated for a conventional low-albedo C-type asteroid surrounded by a dust exosphere, which is normalized to a value at a wavelength of 0.55 μm. The values of the exosphere optical thickness τ, the sizes of individual particles $R_{\rm eff}$ and monomers in aggregates r, and the designations of substances adopted in the models are indicated on the plots and in the captions to them. These spectra were calculated for a phase angle $\alpha = 10°$. It should be noted that varying the phase angle from 0° to ~ 30° has little effect on the shape of the model spectrum, since the phase functions of the considered aggregates and submicron homogeneous spherical particles in the back-scattering region do not contain rapidly-changing details, and the reflection by the surface is assumed to be isotropic.

Figures 13 and 14 present the model spectra $B_{\rm norm}(\lambda)$ for cases when the exosphere contains homogeneous polydisperse submicron particles. Figure 13 shows how different the reflectance spectrum of an active asteroid can be depending on the composition of exospheric particles. It is apparent that the presence of submicron particles of nonabsorbing ice or weakly absorbing astronomical silicates significantly enhances the short-wavelength part of the spectrum $B_{\rm norm}(\lambda)$, while the presence of submicron particles absorbing radiation at short wavelengths has the opposite effect. With an increase in the optical thickness of the exosphere to $\tau \approx 2$, the variation in the spectrum shape becomes more pronounced (Fig. 14). A further increase in τ generally affects the shape of the spectrum less and less, while an increase in multiple scattering in the exosphere containing nonabsorbing or weakly absorbing particles makes the rise in $B_{\rm norm}$ in the short-wavelength range less significant.

To give the reader an idea of what concentration of particles in the exosphere can provide significant changes in the shape of the asteroid's reflectance spectrum, shown in Fig. 13, we present approximate values of the number of particles n_0 in the column of the exosphere layer, directly related to the value of the optical thickness. If we assume for simplicity that the exospheric layer of optical thickness $\tau = 0.5$ (at a wavelength of 0.55 μm) is uniform, and the concentration does not change with altitude, the corresponding number of dust particle on the line of sight is $n_0 \approx 125 \times 10^8$, 26×10^8, 20×10^8, and 18×10^8 cm^{-2} for particles of water ice, astronomical silicates, olivines, and refractory organics, respectively, at $R_{\rm eff} = 0.1$ μm. Note that, based on the n_0 values, the mass of an exospheric cloud of a certain size can be roughly estimated: for a cloud 10 km in diameter consisting of particles of astronomical silicates ($R_{\rm eff} = 0.1$ μm), we obtain its mass of approximately 2.5×10^7 kg, which agrees, for example, with the estimated mass of the dust tail of the active asteroid 248370 (2005 QN173) 4.2×10^7 kg ([129]).

[7] URL: http://smass.mit.edU/data/smass/smass2/a000145.2.txt. Accessed July 14, 2024.

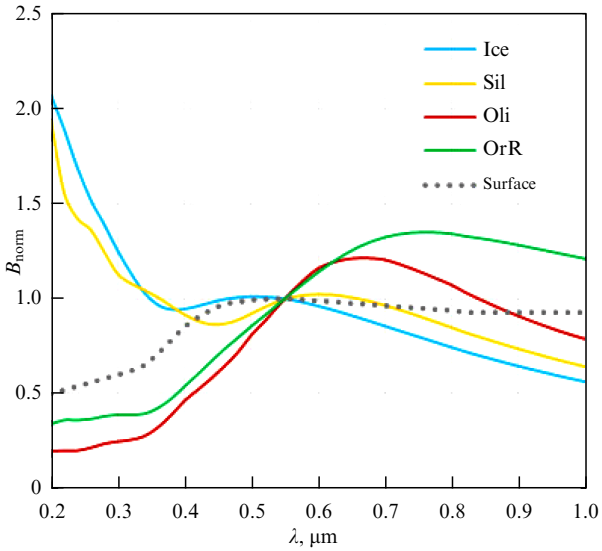

Figure 13. Spectra $B_{\rm norm}(\lambda)$ of a conventional low-albedo asteroid surrounded by a dust exosphere with optical thickness $\tau = 0.5$, which consists of homogeneous submicron particles ($R_{\rm eff} = 0.1$ μm).

Examples of the reflectance spectra $B_{\rm norm}(\lambda)$ calculated for active asteroids with an exosphere containing aggregate particles with monomers of different sizes and various compositions are shown in Fig. 15a and 15b. Comparing the spectra in these figures with the $F(\alpha = 0°)$ spectra in Fig. 11 shows that, in general, the behavior of $B_{\rm norm}(\lambda)$ follows the spectral curves for the single scattering phase function. For example, the positions of the extrema in the spectrum $B_{\rm norm}(\lambda)$ for the exosphere containing ice aggregate particles (Fig. 15a) and in the $F(\alpha = 0°)$ spectrum for aggregates consisting of grains of the same size (Fig. 11a) coincide, and the entire interference pattern shifts to the longer wavelengths with an increase in the size of the monomers. Moreover, it is clear that the difference in the number of monomers in the aggregates (50 and 100 in Figs 11a and 15a, respectively) does not affect the position of the extrema. It should be noted that calculations of $B_{\rm norm}(\lambda)$ for a wide range of parameters of aggregate particles also showed that, for most models for aggregates with smaller grains, the decrease in the spectrum $B_{\rm norm}(\lambda)$ at $\lambda > 0.6$ μm is more significant than for aggregates with larger grains [117].

Figure 15b clearly shows that details of the $B_{\rm norm}(\lambda)$ spectrum are shifted toward the long-wavelength region with an increase in the real part of the refractive index $m_{\rm r}$ of aggregate particles in the exosphere: for astronomical silicates, $m_{\rm r}$ is higher than for H_2O ice, and its main interference minimum λ_1 is shifted relative to λ_1 of ice particles toward longer wavelengths (~ 0.4 μm versus ~ 0.34 μm). It is noteworthy that, in the spectra $B_{\rm norm}(\lambda)$ for those substances the absorption of which increases in the short-wavelength part of the range (olivine and refractory organics; see Fig. 15b), the interference pattern at wavelengths shorter than ~ 0.5 μm is unclear even at $\tau = 0.5$. At the same time, scattering by aggregate particles of ice, which does not absorb radiation, and weakly absorbing astronomical silicates forms clearly visible details in the UV range even at $\tau = 0.1$. It should be noted that, with an increase in the optical thickness of the exosphere to $\tau \approx 2$, the spectral features become more pronounced due to scattering by aggregate particles, but a further increase in τ results in a

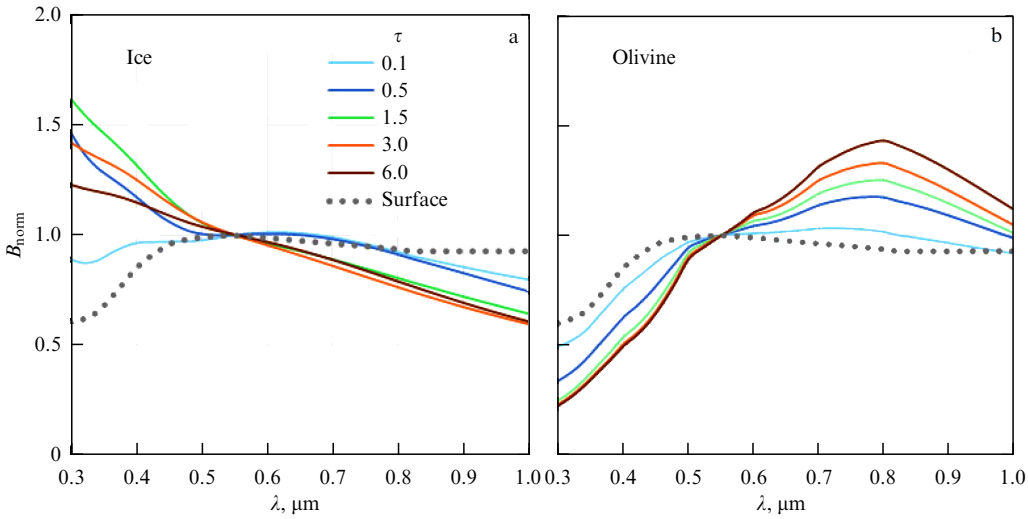

Figure 14. Same as in Fig. 13, but for an exosphere of different optical thicknesses, containing homogeneous particles of H_2O ice (a) and olivine (b) with a size distribution at $R_{eff} = 0.10$ μm and $v_{eff} = 0.10$.

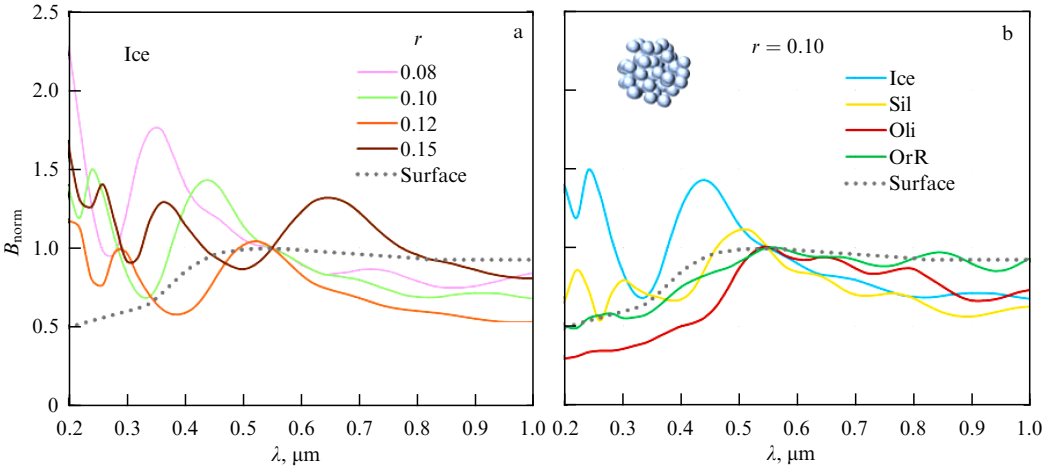

Figure 15. Same as in Fig. 13, but for an exosphere of optical thickness $\tau = 0.5$, which contains H_2O ice aggregates with monomers of different radii (a) and aggregate particles of different compositions with a monomer radius of 0.10 μm (b). Aggregates with porosity of ∼ 0.54 consist of 100 monomers (structure is shown schematically in panel b).

weaker effect, which can change sign with an increase in the contribution of multiple scattering [117].

2.2.4 Options for assessing properties of particles in the exosphere of an active asteroid based on normalized reflectance spectra in visible and UV ranges. It should be recalled that the method of measuring the reflectance spectra discussed in this review made it possible to obtain normalized values of the brightness of objects rather than absolute ones. This circumstance limits the possibilities of their interpretation and does not allow the mass of the scattering cloud of particles to be estimated based on its contribution to the change in the absolute brightness of the object, as was done in [130]. Nevertheless, based on model calculations, on observed variations in the shape of the normalized reflectance spectra of active asteroids, and on the appearance of spectral features that are unusual for solid surfaces, certain conclusions can be drawn about the properties of particles in the exosphere of an active asteroid.

The reflectance spectra calculated for an active asteroid surrounded by an optically thin exosphere containing submicron particles, both homogeneous and aggregate, provide an insight into the way the scattering of light in the exosphere can change the canonical reflectance spectrum of an asteroid and the features of the measured spectra that should be taken into account when interpreting these spectra.

Light scattering by aggregate particles of the exosphere forms interference features in the short-wavelength part of the reflectance spectrum ($\lambda < 0.6$ μm) in the considered range of parameters of the constituent grains, based on the position of which the sizes of constituent grains in the aggregates (but not the aggregates themselves) and the real part of their refractive index can be estimated. However, such estimates cannot be unambiguous, since they are interrelated. Nevertheless, for nonabsorbing or weakly absorbing particles in the exosphere, for which these features are clearly visible in the spectrum, this problem can be solved at least at a qualitative level. In addition, the shape of the measured spectrum at longer wavelengths, which also depends on the properties of the aggregate particles, may facilitate drawing more definite conclusions.

As an example of explaining the details of the measured reflectance spectra, we compare the spectra measured from active asteroids 145 Adeona and 704 Interamnia in 2012 (see Fig. 5) with the model profiles presented in Fig. 15. Two maxima in the spectrum of asteroid 145 Adeona or 'steps' in the spectrum of asteroid Interamnia (at approximately 0.4 and 0.5 μm) and a decrease in the spectrum towards longer wavelengths suggest that the particles in the exospheres formed in these active asteroids were most likely aggregates and consisted of weakly absorbing grains with a radius of about 0.1 μm or less. Moreover, since the distance between the indicated features in the measured spectra is significantly smaller than the distance between the interference maxima in the model spectra for aggregate particles of any individual substance, it can be assumed that such features appeared in the spectrum due to scattering by particles of different compositions, for example, ice and silicates (see [68]).

The spectra calculated for an exosphere containing aggregates of particles absorbing radiation in the short-wavelength range (which is typical of many substances that might be expected to be found on an asteroid) show that absorption significantly weakens the interference features in this range. Therefore, attempts to detect strongly absorbing particles in the exosphere, and even more so to estimate their properties from such features in the spectrum, cannot be successful.

Light scattering by homogeneous particles significantly smaller than the wavelength manifests itself in the spectrum of an active asteroid, as expected, by a stable increase in intensity at wavelengths less than 0.4–0.5 μm, provided that absorption in this range is weak. The presence of absorbing particles of such sizes in the exosphere does not introduce any fundamental changes into the shape of the normalized reflectance spectrum of an active asteroid.

Thus, model calculations show that it is possible to detect the presence of an exosphere and estimate the properties of its particles based on details of the normalized reflectance spectrum of an active asteroid under the following conditions:

(1) The exosphere contains nonabsorbing or weakly absorbing particles.

(2) The spectra of an active asteroid can be measured at wavelengths shorter than $\lambda \sim 0.5$ μm, and especially in the UV range.

It should be taken into account that it is not possible to unambiguously estimate the concentration of particles in a real exosphere containing particles of different compositions and morphologies based on the magnitude of the rise in the normalized reflectance spectrum of an active asteroid at short wavelengths or on the extent to which the emerging details are pronounced. The reason is, for example, that the scattering of light by weakly and strongly absorbing particles has a multidirectional effect on the shape of the spectrum (see Figs 13 and 15), and it is possible that numerous absorbing particles may not manifest themselves clearly in the reflectance spectrum, but mask details related to the presence of weakly absorbing particles.

2.2.5 On the option to assess asteroid activity using polarization measurements. To determine the properties of the exosphere of an active asteroid, one can also use polarimetry, a method known for its sensitivity to the characteristics of light-scattering particles. The possible influence of the exosphere formed around an asteroid on the polarization of the light scattered by it, which can be measured in ground-based UBVR observations (wavelengths $\lambda = 0.36, 0.44, 0.54$, and 0.68 μm), was recently estimated on the basis of calculations of the scattering characteristics of particles of various morphologies and compositions [131]. The results of this study are briefly presented below.

In the modeling, the parameters of the exospheric particles were chosen based on an analysis of the reflectance spectra of asteroids in the near and visible UV ranges, which were measured when the asteroids exhibited the signs of sublimation activity (see references above). However, unlike the modeling of the reflectance spectra, in calculations of polarization, the nonspherical shape of homogeneous particles was taken into account. They were represented by a mixture of randomly oriented spheroids with various ratios of axes ($E = 0.7-1.3$). The calculations were made using the T-matrix method [114] for polydisperse particle ensembles at two values of the effective radius of the equivalent volume sphere $R_{\text{eff}} = 0.1$ and 1.0 μm and with an effective variance $v_{\text{eff}} = 0.05$.

The main polarimetric characteristic of a scattering medium, on the basis of which its properties are estimated, is the phase dependence of the degree of linear polarization in a wide range of phase angles $P(\alpha)$. Its behavior is determined by the properties of scatterers in the medium: their sizes, morphology, refractive index, and packing density (see, for example, [132] and references therein). To determine the properties of particles in the optically thin exosphere of an active asteroid on the basis of the measured dependence $P(\alpha)$, it is necessary to take into account the polarization of light reflected from the surface of the asteroid. In these calculations, the dependence $P(\alpha)$ for the surface of an active asteroid was taken to be the same at different wavelengths, since it was required to only track the changes that the exosphere can introduce into the observed characteristics of the active asteroid. For a conventional asteroid, the intensity and polarization of light scattered by the surface were calculated on the basis of the scattering matrix of aggregate silicate particles (see details in [131]). This gave a weak branch of negative polarization at phase angles less than $\sim 20^\circ$ and a polarization maximum of $\sim 26\%$ at a geometric albedo of the object $A_g \approx 0.1$ (Fig. 16), which corresponds to the characteristics of low-albedo asteroids.

Figure 16 shows how light scattering in the exosphere, consisting of small homogeneous particles, can alter the phase function of the linear polarization of light $P(\alpha)$ reflected by the model asteroid. Presented are models for particles of different compositions at two wavelengths, $\lambda = 0.36$ and 0.54 μm (channels U and V), and a model curve for the asteroid surface. It can be seen that the size of the scattering particles of the exosphere relative to the wavelength largely determines their influence on $P(\alpha)$ of the active asteroid. If particles are significantly smaller than the wavelength ($R_{\text{eff}} = 0.1$ μm and $\lambda = 0.54$ μm), light scattering in the exosphere enhances the positive polarization in the entire range of phase angles and suppresses the weak branch of negative polarization characteristic of the surface of asteroids. This is explained by the fact that the light scattered by particles of such sizes is polarized predominantly in the plane perpendicular to the scattering plane, and $P(\alpha)$ has a bell-shaped form with a high maximum at $\alpha \approx 90^\circ$ weakly depending on the particle material (see, for example, [114]). With an increase in size of particles, the effect of the refractive index on polarization

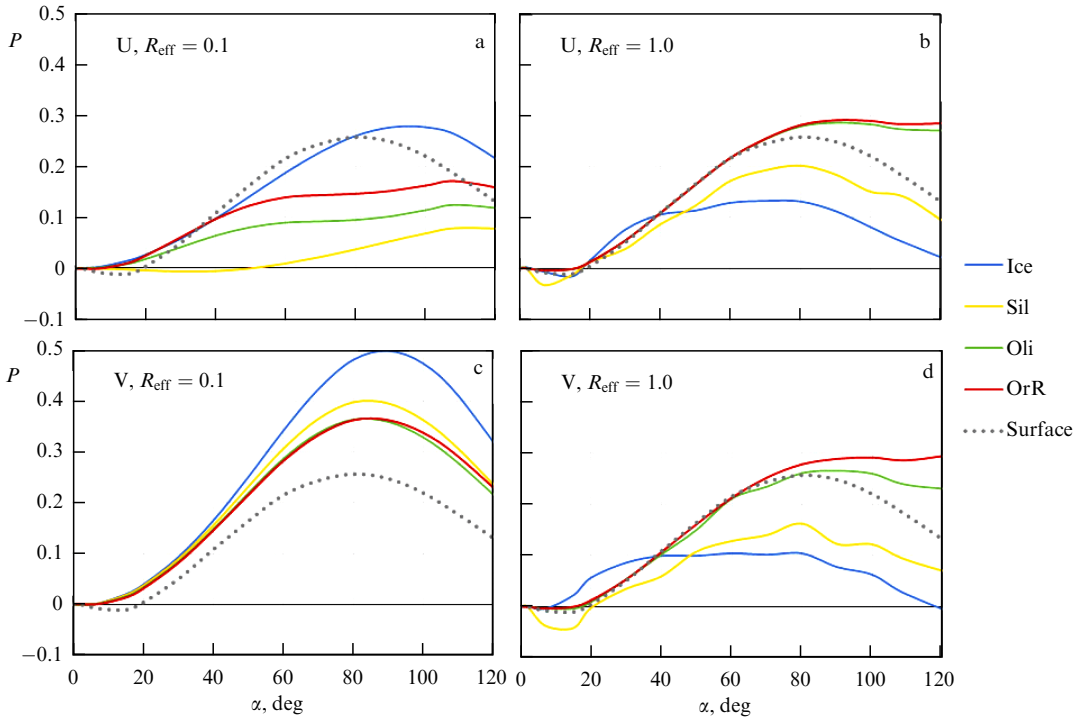

Figure 16. Degree of linear polarization of light P reflected by a model asteroid with an exosphere at wavelengths of 0.36 and 0.54 μm (channels U and V, respectively), depending on phase angle of observations α. Displayed are models for particles of different compositions and sizes R_{eff} (in microns) and a model for an asteroid without an exosphere ('Surface'). The optical thickness of an exosphere is taken to be $\tau = 0.5$ at $\lambda = 0.54$ μm.

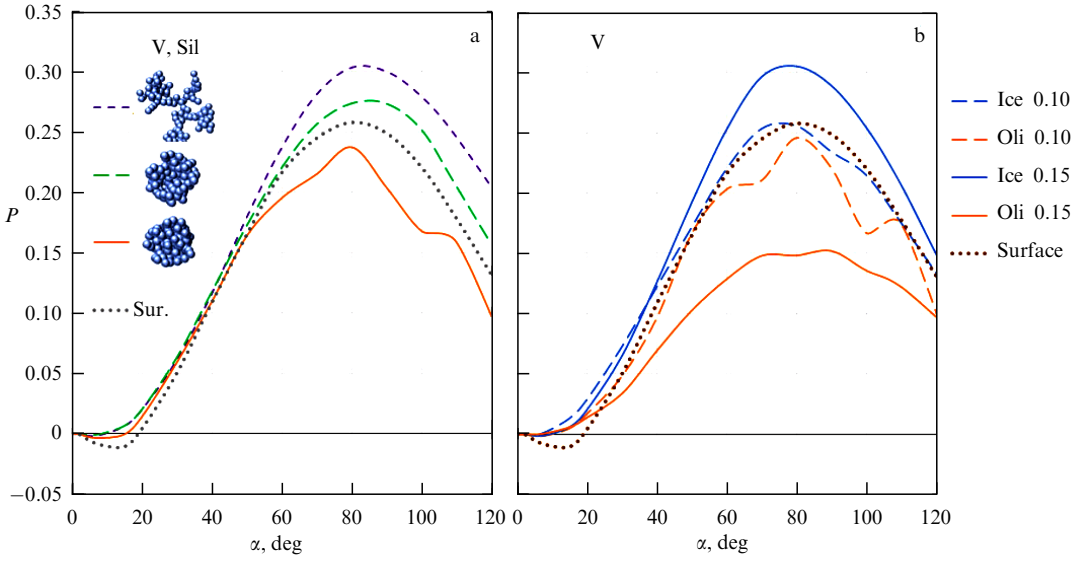

Figure 17. Degree of linear polarization of light P reflected by a model asteroid with an exosphere of optical thickness 0.5 at $\lambda = 0.54$ μm consisting of particles — randomly oriented aggregates ($N = 100$ monomers of size r) — depending on phase angle α: (a) dependences for structures of various porosities (0.54, 0.72, and 0.94 (from bottom to top)) consisting of astronomical silicates at $r = 0.10$ μm; (b) models for aggregate particles of ice and olivine (porosity ~ 0.54) consisting of monomers of the indicated radii (in microns).

increases; the shape of $P(\alpha)$ becomes more complex, and its maximum is significantly reduced. As a result, the positive polarization of light reflected by an asteroid with an exosphere consisting of relatively large weakly absorbing particles becomes lower than that of an asteroid without an exosphere, and the negative branch of polarization can become more pronounced. At the same time, the presence of relatively large absorbing particles in the exosphere changes the dependence $P(\alpha)$ of the asteroid only slightly.

Figure 17 gives an idea of the effect of scattering by aggregate particles present in the exosphere on the $P(\alpha)$ of an active asteroid. As an example, we show the functions $P(\alpha)$ calculated for aggregate particles of different porosities, consisting of astronomical silicates with a monomer radius of 0.10 μm, and for relatively dense aggregates consisting of nonabsorbing ice and absorbing olivine monomers of the indicated sizes. It is apparent that the behavior of $P(\alpha)$ of an active asteroid depends both on the refractive index and

structure of the particles in the exosphere and on the sizes of the monomers composing the aggregates. The function $P(\alpha)$ for an active asteroid with an exosphere containing ice aggregate particles, in general, follows the behavior of $P(\alpha)$ for an asteroid without an exosphere, but often takes on higher values and does not have a negative branch. When the exosphere contains absorbing aggregate particles, the function $P(\alpha)$ behaves similarly if the aggregate structure is loose, but may have a more complex appearance for a close-packed structure.

Thus, light scattering in the exosphere of an active asteroid can both weaken the polarization of light reflected from the surface and lead to its enhancement, depending on the wavelength, range of phase angles, substance, and morphology of particles in the exosphere. Light scattering in the exosphere can also change the spectral gradient of polarization towards both more positive and negative values.

At phase angles less than 30°, typical of observations of Main Belt asteroids, the changes introduced by scattering in the exosphere into the polarization of an active asteroid are small and differ little for particles of different properties. In this regard, the prospects for determining the characteristics of exospheric particles based on polarimetric data at small phase angles seem very adverse. Nevertheless, a change in the negative branch of polarization compared to the canonical values should indicate the development of an exosphere in an active asteroid.

At phase angles greater than 30°, the effect of scattering in the exosphere on the polarization of an active asteroid may be more noticeable, which makes promising the use of polarimetry to study the activity of near-Earth asteroids. This effect should also be taken into account when estimating the albedo of an asteroid from the polarization maximum (according to Umov's law) if this asteroid can be expected to exhibit activity.

2.3 Influence of solar events on sublimation-driven dust activity and other manifestations of asteroid activity

In studying the spectral characteristics of active asteroids, we discussed above the possible influence of the solar wind, flares, and eruptive events on the Sun on the dust activity of asteroids in general and on primitive asteroids in particular ([67, 93] and references therein). Here, we only note that the time of propagation of a weak shock wave formed in the solar wind plasma to any asteroid is determined by the average speed of the slow solar wind (~ 550 km s^{-1}; see, for example, [133, 134]). However, according to data from the GOES-16 and SOHO satellites, more powerful shock waves, as a consequence of coronal mass ejections on the Sun, can propagate at a speed 1.5 to 2 times higher.[8]

In addition to Figs 18 and 7 displaying the reflectivity spectra of active asteroids 24 Themis, 704 Interamnia, and 449 Hamburga, we present a diagram (Fig. 19) illustrating the supposed 'sweeping away' of their dust exospheres on March 18, 2019. It could have occurred when the asteroids were exposed to two shock waves (ICME1 and ICME2, shown in Fig. 19), close in time (with an interval of ~ 35 hours) and power, which arose during coronal mass ejections on the Sun, CME1 (2019-03-08) and CME2 (2019-03-09), with a power slightly exceeding the minimum for such events, between which two weaker waves occurred.[9]

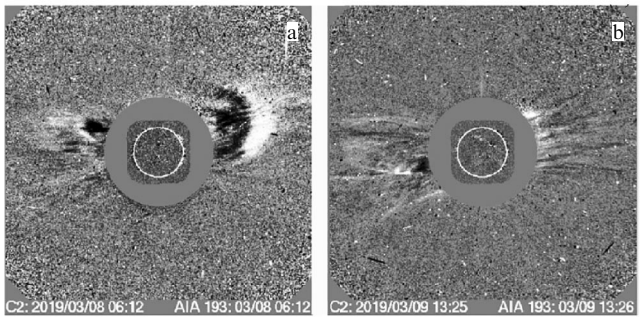

Figure 18. Coronal mass ejections CME1 (a) and CME2 (b) detected by spectral coronagraph (LASCO) aboard Solar and Heliospheric Observatory (SOHO). It is seen that CME1 and CME2 are close to equatorial plane of Sun and probably caused formation of shock waves in interplanetary medium (ICME1 and ICME2), which led to simultaneous temporary removal of DE of active asteroids 24 Themis, 449 Hamburga, and 704 Interamnia on March 18, 2019.

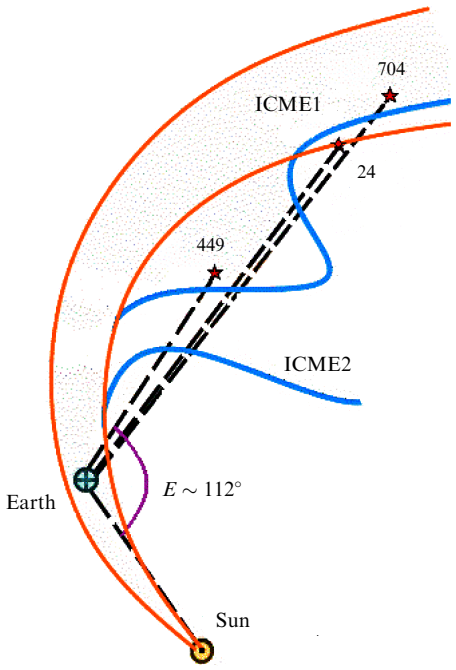

Figure 19. Location of asteroids 24 Themis, 449 Hamburga, and 704 Interamnia at very close elongation angles ($E \sim 112°$), determining their location in relation to observer and Sun during their observations from March 17, 2019 to April 4, 2019. Proposed orientation of fronts of close-in-time shock waves (shown in blue) in solar wind caused by coronal mass ejections on Sun on March 8, 2019 and March 9, 2019. Spiral lines of force of solar magnetic field shown in orange. (Figure adapted from [67].)

It is of importance to keep in mind that these eruptive events occurred near the minimum of the 11-year cycle of solar activity, against the 'background' of its long quiescent state. As noted above, the temporary removal of the DE of the active asteroids 24 Themis, 704 Interamnia, and 449 Hamburga on March 18, 2019 is confirmed by its simultaneous restoration on March 19 for all three asteroids. Other fairly

[8] URL: https://cdaw.gsfc.nasa.gov/CME_list. Accessed July 14, 2024.

[9] URL: https://cdaw.gsfc.nasa.gov/CME_list/UNIVERSAL_ver2/2019_03/univ2019_03.html. Accessed July 14, 2024.

convincing evidence of this event is the following circumstances, which significantly increase its probability:

(1) The two main coronal ejections are predominantly directed in the plane of the Sun's equator, in which the asteroids under consideration are also located (Fig. 18).

(2) The ejected mass of the stronger first ejection is predominantly asymmetric towards all three asteroids, which have practically coinciding elongation angles (Fig. 19).

The unusual similarity in the shape of the approximated reflectivity spectra of 24 Themis, 449 Hamburga, and 704 Interamnia from March 17 to 20, 2019 has attracted attention. This can be explained by the fact that the values of the asteroid elongation angles ($E \sim 112°$) almost coincide (Fig. 19), and the phase angles of observations, determining the location of these bodies relative to the observer and the Sun, are close, which implies that the conditions for recording their spectra are also similar. On the other hand, the reason for such similarity could also be the general low-perturbed state of the interplanetary plasma and the solar magnetic field, extending to tens of astronomical units, during the period of minimum solar activity.

We now discuss in more detail the regular spectral feature in the form of a 'comb,' which we first detected in the reflectance spectra of three of the eight observed primitive asteroids — 177 Irma, 203 Pompeja, and 383 Janina — probably under the influence of more powerful events on the Sun at the end of November 2020. As reported above, the asteroids were influenced by a significant solar flare (in the range of classes M–X in the X-ray range) and the associated CME[10] (Fig. 20). At the same time, the said spectral feature was formed during a period of comparatively low overall solar activity and, perhaps for this reason, it was noticed by us. This implies that, during the approximately ten days that elapsed between the solar flare and the CME and our observations of the asteroids, there were no other similar events. It should be added that, although all the asteroids were exposed to a solar X-ray flare ten days before our observations, it is possible that the shock waves due to the CME had not yet reached the asteroids. An image of this event shows that, despite the orientation of the CME along the solar equator, its vector was directed predominantly to the west, i.e., away from the asteroids (see Fig. 20). Consequently, the shock waves caused by this CME could have reached the asteroids much later — indirectly rather than directly, moving along the spiral lines of force of the solar magnetic field.

The elongation angles of asteroids 177 Irma, 203 Pompeja, and 383 Janina were also in a fairly narrow sector ($\sim 30°$ and on average about 160°) [92], which probably ensured similar conditions for their observations from December 7 to 14, 2020, compared to other asteroids in this group. In addition, they exhibited the most significant deviations from their spectral 'templates' (Fig. 8c, d, e). An unusual wave-like feature in the form of a 'comb' in the red part of the reflectance spectra, probably of an interference nature, is weakly noticeable in 177 Irma, but is quite clearly visible with a more significant amplitude in all three consecutive spectra of two other asteroids (obtained at time intervals from ~ 40 min to an hour) — 203 Pompeja and 383 Janina — which confirms its reliability. Interpretation of these features requires further model calculations.

[10] URL: https://cdaw.gsfc.nasa.gov/movie/make_javamovie.php?date=20201129. Accessed July 14, 2024.

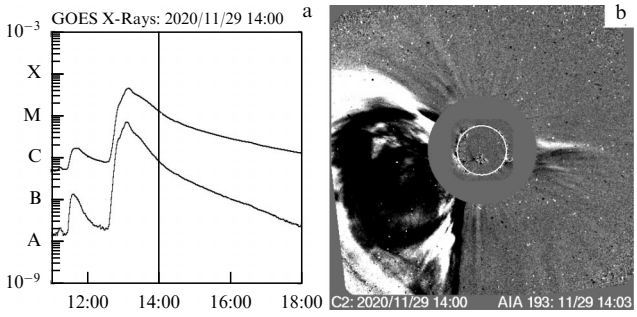

Figure 20. (a) Solar flare in X-ray range on November 29, 2020 and (b) associated coronal mass ejection near Sun's equatorial plane (see reference in text).

2.4 Section conclusions

The following conclusions can be drawn in Section 2:

(1) We have clarified SDA concepts for primitive asteroids, demonstrating that sublimation ejects predominantly submicron dust particles.

(2) The feasibility of spectral detection of the SDA of primitive asteroids below the limit of spatial resolution of asteroid activity signs in their direct images has been substantiated.

(3) March 2019 spectra of 24 Themis, 449 Hamburga, and 704 Interamnia revealed, for the first time, quasi-simultaneous shock-wave passages from closely spaced weak CMEs.

(4) Over a period of approximately a decade, as a result of spectral surveys of ~ 300 primitive asteroids with orbital eccentricities of at least 0.1 (which undergo more significant changes in subsolar temperatures on the surface when moving from aphelion to perihelion), 16 active asteroids and 16 suspected of being active were discovered near perihelion distances.

(5) Qualitative (based on the occurrence of a significant negative gradient of the reflectance spectrum of an asteroid in an active state compared to the gradient of its 'classical' reflectance spectrum in an inactive state) and quantitative (based on the positive value of the differences among root-mean-square errors in the intensity of the luminous flux recorded in the U band from an active asteroid and a nonvariable control star and a 'signal-to-noise' ratio of an asteroid of at least several ten) criteria for detecting SDA of primitive asteroids as an indicator of the presence of water ice in their matter were established.

(6) An asteroid's SDA signatures may become noticeable due to a sufficiently large number of small scattering particles in its exosphere. The greatest contribution to the spectral manifestations in the UV and visible ranges is made by weakly absorbing particles ~ 0.1 μm in size and their aggregates.

(7) Analysis of the activity of asteroids themselves suggests that they can also be used as indicators of flare and eruptive events on the Sun. Data from the GOES-16 and SOHO satellites show that CMEs are the main source of shock waves in the solar wind (ICMEs), which, during the period of minimum solar activity, primarily move at a speed close to that of the slow solar wind and are directed quite close to the plane of the solar equator. This is confirmed by their detection using the reflectivity spectra of 24 Themis, 449 Hamburga, and 704 Interamnia in March 2019.

(8) Future studies of solar-event effects on active asteroids must consider primary CME energy, speed, and

geometry, alongside ICME propagation modelling in the heliospheric magnetic field.

3. Asteroid collisions as a mechanism of sublimation-driven dust activity of asteroids

As noted in Section 1.1, the ejection of particles from the surface of an asteroid can be driven by two main mechanisms: ejection upon impact (collisional mechanism) and sublimation (collisional-sublimation, comet-like). The sublimation mechanism requires the presence of open ice on the surface of the asteroid and a corresponding influx of energy from the Sun. The collisional mechanism is more universal: it does not require the presence of ice. Almost any impact ejects particles of the target asteroid into the near-asteroid (interplanetary) space. Moreover, a collision can expose subsurface ice and thus provide conditions for sublimation activity. The dusty exosphere of an asteroid formed upon impact, consisting of small dust particles, dissipates relatively quickly (on the dynamic scale of the movement of the ejected particles), so such structures are not so easy to detect. Sublimation activity can manifest itself for a longer period of time, while the asteroid is in the perihelion zone. To determine the relative contribution of the described mechanisms to SDA, they need to be compared, preferably at a quantitative level. To solve this problem, it is necessary to obtain estimates of the following characteristics:

(1) Frequency and velocity of asteroid collisions in the MAB.

(2) Parameters of ejecta formed during collisions.

(3) Frequency of SDA events: model estimates and comparison with observations.

3.1 Frequency and velocity of asteroid collisions in Main Asteroid Belt

Estimates of the collision rate of objects in the MAB are based on theoretical models rather than rare observations of the aftermath of collisions. The basic analytical theory for calculating the frequency and velocity of collisions, which was developed in studies [135, 136], was applied by many researchers in subsequent years (see, for example, [137–139]). Alternatively, various authors (see, for example, [139, 140] and references in review [141]) use a direct numerical approach based on integrating the orbits of asteroids over a sufficiently long period of time. The resulting distribution of the number of encounters and mutual velocities during encounters can be used to determine the probability of collisions and characteristic impact velocities. The average number of collisions $N_{\rm col}$ between a target asteroid of radius $r_{\rm t}$ and impactor asteroids with a radius greater than $r_{\rm p}$ over time Δt is usually estimated using an equation in the form (see, for example, [42])

$$\left\langle N_{\rm col}(>r_{\rm p})\right\rangle = \langle P_{\rm i}\rangle (r_{\rm t}+r_{\rm p})^2 \Delta t N_{\rm p}(>r_{\rm p})\,, \qquad (2)$$

where $N_{\rm p}(>r_{\rm p})$ is the number of impactor asteroids with a radius greater than $r_{\rm p}$, and $P_{\rm i}$ is the average internal probability of a collision between the target and the population of impactors. The formula is applicable provided $r_{\rm p} \ll r_{\rm t}$. $P_{\rm i}$ is usually measured in units of [km^{-2} year^{-1}]. $P_{\rm i}$ can be considered for specific ensembles. Such calculations were made in [143]. The $P_{\rm i}$ values for the probability of collisions between asteroids belonging to different MAB zones vary from 0.35×10^{-18} km^{-2} year^{-1} for collisions between outer zone asteroids (values of semi-major axis a in the range of 3.3–3.51 AU) and inner zone asteroids (2.1–2.5 AU) to 11.98×10^{-18} km^{-2} year^{-1} for collisions between inner zone asteroids. According to the results of [143], the estimated total probability of collision with asteroids of all zones is 21.5×10^{-18} km^{-2} year^{-1}.

It is clear that to estimate the number of sufficiently effective collisions, it is necessary to know the distribution of asteroids both by size and by approach velocities, i.e., by energy. 'Efficient enough' means that the impact ejects an amount of dust from the target asteroid that provides observable manifestations, or subsurface (ice-containing) layers are exposed over a sufficiently large area of the target asteroid, and subsequent manifestations of the comet-like mechanism are noticeable.

To estimate the velocity of encounter (collision), the observational estimate of the random (relative to circular motion) velocity can be used. According to [144], the random velocity $V_{\rm ran}$ is estimated from

$$V_{\rm ran} = (e^2+i^2)^{1/2} V_{\rm kep}\,, \qquad (3)$$

where $V_{\rm kep}$ is the Keplerian velocity, e is the eccentricity, and i is the orbital inclination (in radians). The root-mean-square value of random velocities for the MAB as a whole is about 4.8 km s^{-1}. This estimate agrees well with the results of dynamic modeling (numerical model of MAB asteroid encounters) presented in [143].

For an ensemble of impactor asteroids, it is necessary to know the distribution of their random velocities. In [145], based on data of the Minor Planet Center on the orbital elements of 1,178,752 MAB asteroids and formula (3), a distribution of $V_{\rm ran}$ was derived, or, more precisely, a distribution of $p(v)$: the relative number of asteroids in a velocity interval 1 km s^{-1} wide and centered on the value of $V_{\rm ran}$. This distribution is displayed in Fig. 21. It is of interest that it is well described by the approximation formula

$$p(v) = 0.27\exp\left(\frac{-(v-3.1)^2}{1.62}\right) + 0.12\exp\left(\frac{-(v-5.0)^2}{1.28}\right) + 0.03\exp\left(\frac{-(v-7.0)^2}{8.0}\right). \qquad (4)$$

It is easy to verify that $\int_0^{20\ {\rm km/s}} p(v)\,{\rm d}v \approx 1$. It is characteristic that the formula for $p(v)$ is described by a set of Gaussian functions. This may indicate that the field of mutual velocities of Main Belt asteroids is formed as a result of random processes.

Since an ensemble of asteroids is examined, it is necessary to know the size distribution of asteroids (both impactors and targets). Usually, the cumulative form of the distribution $N(>D)$ is used, i.e., the number of asteroids with a diameter exceeding a given value D. Since observations (detection) of MAB asteroids are currently complete only for asteroids with a diameter $D > 1$ km, for smaller asteroids the size distribution remains a subject of modeling. Usually, the distribution is specified in the power form $N(>D) \propto D^{-q}$. To date, the problem of deriving a more or less generally accepted distribution in a given size range ($D < 1$ km) has remained unsolved, and the variety of available models, unfortunately, implies a variety of results. According to the table from [146], for asteroids of size $D < 1$ km, different authors give q values ranging from 1.1 to 4.4! In Figure 22, adapted from the

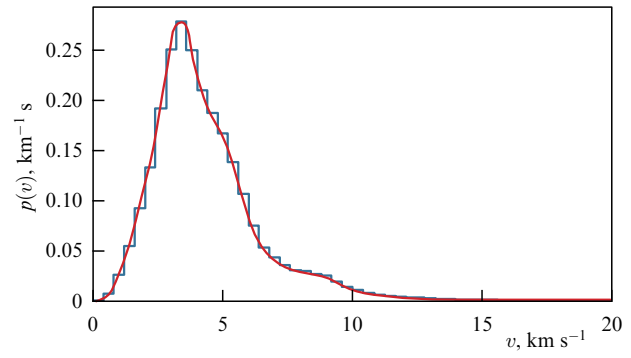

Figure 21. Distribution of $p(v)$ for MAB asteroid sample (from [145]) and approximation function calculated using Eqn (4) (red curve).

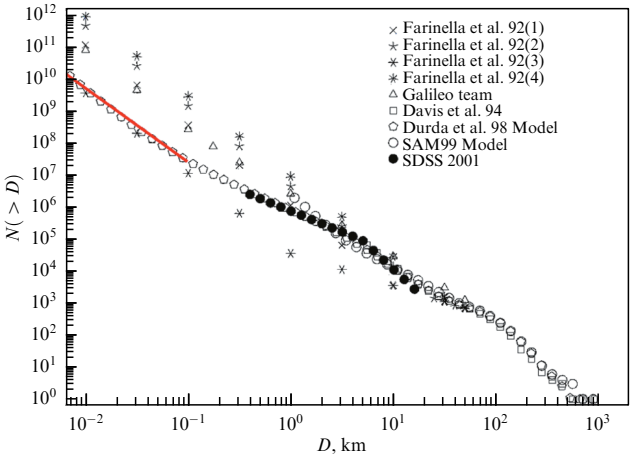

Figure 22. Cumulative size distribution of MAB asteroids (diameter D). Red line approximates model distribution of asteroids $N(>D) \propto D^{-2.3}$ for $D < 100$ m.

classical review [147], the spread of $N(>D)$ values for $D \sim 10$ m is as large as two orders of magnitude. In our studies [145, 148] for asteroids with a diameter of less than 100 m, it is accepted that $q = 2.3$ (the specific form of dependence $N(>D) = 8.4 \times 10^{11} D^{-2.3}$, where D is measured in meters).

The situation with the size distribution of NEAs is similar. Wherever information is incomplete (it is believed that at present the sample of NEAs with a diameter of more than 0.7 km is considered complete, i.e., almost all NEAs of such sizes have been observed), models are used, the spread between which is significant among different authors. Figure 23a shows the cumulative distribution of NEAs by absolute asteroidal stellar magnitude H and, consequently, by size — diameter D. The values of D and H are related by the formula $D = 10^{3.1236-0.5\log_{10}(A)-0.2H}$ [149], where A is the albedo. When plotting Fig. 23, some average value $A = 0.15$ was taken.

To model the population of NEAs (more precisely, the population of NEOs — near-Earth objects, which include NEAs and a small number of comets) — the model (software package) NEOPOP developed by the European Space Agency (see [150, 151]) is often used. As part of activities related to the ESA's Space Situational Awareness (SSA) program, a need arose for a software tool for modeling NEA observation systems; the open-source Near-Earth Object Population Observation Program (NEOPOP) was developed, which enables users to:

- generate NEO populations based on the model [151];
- simulate NEO population observations;
- analyze NEO populations.

NEOPOP is implemented as a console program and can be conveniently controlled using a graphical user interface (GUI).

Recently, the NEOPOP model has been significantly modified. The NEOMOD model was developed (see [152, 153]), which approximates the distribution of real asteroids more accurately. Figure 23 shows the distributions of low-mass NEAs according to the NEOPOP and NEOMOD models. As can be seen from the figure, the difference in the distributions between these two popular models is quite significant.

3.2 Parameters of ejecta formed during collisions

Figure 24a illustrates the basic picture of particle ejection during a collision of an impactor asteroid with a (more massive) target asteroid. The thickness and density of the arrows correspond to the size and number of particles and illustrate the fact that large particles (thicker arrows) number

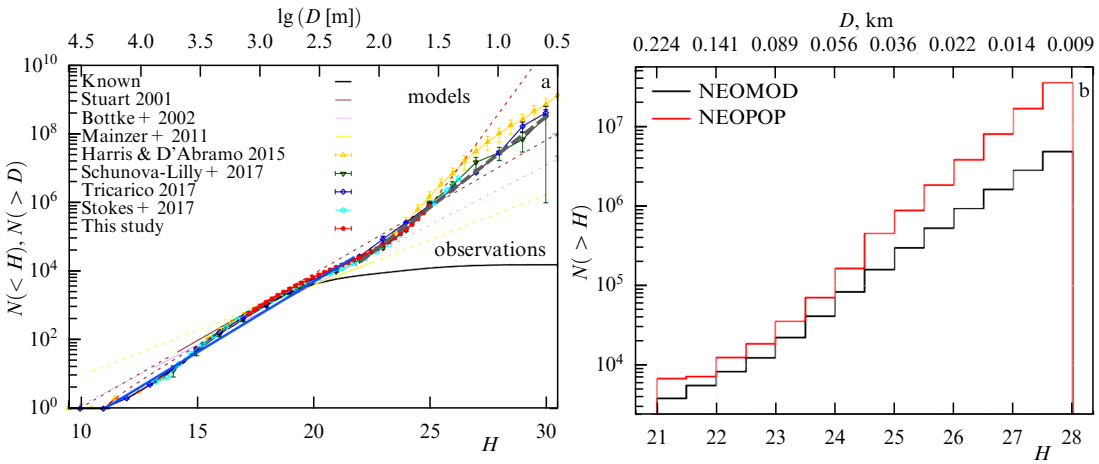

Figure 23. (a) Cumulative size distribution of NEAs (diameter D) and absolute asteroidal stellar magnitude H. (b) The same according to NEOPOP (red line) and NEOMOD (black line) models. For asteroids smaller than 0.7 km, observed number of asteroids is significantly less than that predicted by the models.

fewer than small ones (thinner arrows). The length of the arrows illustrates the dependence of the ejection velocity on the size of the ejected particles. Figure 24b shows the velocity field of fragments formed during the bombardment of a basalt target in a laboratory experiment [154] (see below for more details on this experiment).

The collision results in the ejection of matter into a cone with total opening angle α. Statistics on the sizes of craters from ground explosions are given in [155]. The range of explosion energies is fairly wide: from 1 t to 5 kt of TNT equivalent. The craters are characterized by the following parameters: in soft rocks, the h_c/D_c ratio, where h_c and D_c are the depth and diameter of the crater, respectively, is approximately 0.27, while in harder fractured rocks, it is 0.23. With a conventional conical shape of the crater, this gives full opening angles $\alpha = 122^\circ$ and 131°, respectively. According to [156], the depth of a natural terrestrial impact crater is related to the crater diameter by the ratio $h_c/D_c = 0.20$. Observations of ensembles of craters of approximately the same age on the same asteroid yield a spread, caused primarily by differences in the properties of areas of the asteroid's surface. According to [157], the h_c/D_c distribution for an ensemble of approximately 500 craters in the size range from 3 to 63 km on the asteroid 4 Vesta corresponds to a Gaussian distribution in the range of 0.05–0.4, with a maximum of 0.18. In what follows, we adopt this value. In the full-scale space experiment DART, the angle of the ejecta cone was found to be $125^\circ \pm 10^\circ$ [158]. Classical study [159], which generalizes the vast experience of full-scale and theoretical experiments, has shown that the calculated ejection velocities are insensitive to the ejection angle. Therefore, in the modeling, a simple scheme of ejection into a hemisphere ($\alpha = 180^\circ$) with one velocity (for a given particle size) can be adopted.

During a collision, a substance with mass M_c is ejected from the crater. It can be estimated, assuming a conical structure of the crater: $M_c = (\pi/18) \times D_c^2 h_c \rho_t$, where ρ_t is the average density of the target. The crater size depends on the energy (velocity and mass) of the impactor. The crater is formed on small asteroids (less than ~ 10 km) with a characteristic strength of $Y \sim 1$ kPa and impactors no larger than 100 m, constituting a strength mode (see more details in [145]). The size of such a crater (crater diameter D_c) can be estimated using an expression from [160],

$$D_c = 2.06 r_p \left(\frac{\rho_t V_p^2}{Y}\right)^{0.205} \left(\frac{\rho_p}{\rho_t}\right)^{0.40}, \qquad (5)$$

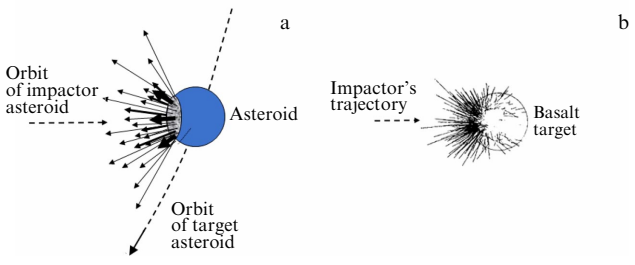

Figure 24. (a) Diagram of particle (fragment) emission from a crater formed during an asteroid collision. (b) Velocity vectors (without arrows) of fragments formed during the bombardment of a basalt target in a laboratory experiment [154].

where r_p and V_p are the radius and velocity of the impactor, and ρ_t and ρ_p are the densities of the target asteroid and the impactor, respectively. The mass M_c of the substance ejected from the crater can be estimated from

$$M_c \approx \frac{0.274 r_p^3 V_p^{1.23} \rho_t^{1.615}}{Y^{0.615}} \left(\frac{\rho_p}{\rho_t}\right)^{1.2} \text{ kg}. \qquad (6)$$

This is an estimation. The dependence on ρ is fairly strong, but the density of asteroids itself does not vary very significantly, within the range of $\sim (1-5) \times 10^3$ kg m^{-3}, so the factor $\rho^{1.615}$ can yield a spread of approximately an order of magnitude. For different substances, variations in strength Y from asteroid to asteroid can be several orders of magnitude (for example, such differences are possible for C and M class asteroids), and the structure of asteroids can also be quite different — from a 'pile of rubble and dust' to a monolith [161]. So the factor $Y^{0.615}$ can also yield a spread of at least an order of magnitude. However, both of the above factors (density and strength) probably operate 'in the opposite direction,' since less dense objects are usually less robust. In general, Eqn (6) can be used for so-called 'order of magnitude' estimates if ρ and Y are not known in advance. For further analysis, we assume that $\rho_p = \rho_t = \rho$. Taking the typical values $\rho = 2000$ kg m^{-3} and $Y = 1$kPa (these estimates are based on the results of space experiments for asteroids 25143 Itokawa, 101955 Bennu, and 162173 Ryugu), we obtain the estimated expression

$$M_c \approx 839 r_p^3 V_p^{1.23} \text{ kg}. \qquad (7)$$

As an example, we estimate the mass of the matter ejected during a collision of a target asteroid with an impactor of size $r_p = 5$ m at a speed of $V_p = 5000$ m s^{-1} to obtain $M_c = 3.72 \times 10^9$ kg. Approximately the same amount of solid matter (dust) is emitted by some comets when passing the perihelion zone. It is interesting to apply Eqn (6) to estimate the mass of the ejecta in the DART experiment. According to [162], at the moment of impact, the mass of the spacecraft, i.e., the impactor, was 580 kg, and the speed was 6.14 km s^{-1}. The authors of [162] estimated the density of the asteroid at 2400 kg m^{-1}. The effective radius of the impactor reduced to this density is 0.73 m. Applying Eqn (6), we obtain $M_c \approx 2.63 \times 10^3$ t. A close a priori estimate (5000 t) is presented in [163]. A posteriori estimates of M_c vary in the range of 1000–10,000 t. In general, it should be repeated that Eqns (6) and (7) can be used to estimate M_c 'by order of magnitude.'

Equation (6) and, consequently, (7) are not applicable over the entire range of impactor sizes and velocities. According to [164] (see, for example, Table 3.3 from the aforementioned classic manual), in the (sub)millimeter range of impactor sizes, the ratio of the ejected mass to the impactor mass is approximately the same as for larger impactors (several thousand), while, for micron-sized impactors, this ratio is close to 1–5. In [165], microcraters were studied in ordinary soda-lime glass bombarded by low-density polystyrene microimpactors (1.06 g cm^{-3}) with masses from 0.7 to 62 pg and velocities from 2 to 14 km s^{-1}. With normal incidence, the total displaced mass M_e of target material per unit of kinetic energy of the projectile slowly increases together with the impactor kinetic energy E as $M_e = 230 E^{1.1}$ pg (here, E is measured in μJ). This formula implies that, when a projectile weighing 50 pg hits a speed of

5 km s^{-1}, a mass of 115 pg is ejected. This must be taken into account when estimating the ejected mass.

Ejection of matter from the parent body at a velocity exceeding the escape velocity results in the formation of a coma of ejected fragments, which initially contains many very small particles (micron and submicron in size). In studies of particle ejections from impacts, the particle size distribution is described by an approximate power-law expression of the form $dn \propto r^{-s_r} dr$, where dn is the number of particles with radii r in the range $[r, r + dr]$ and is characterized by the minimum and maximum sizes (radii) r_{min} and r_{max} and the slope (index) s_r. The power-law spectrum of particle masses looks similar: its index s is related to s_r as $s_r = 3s - 2$. Here, the spectra are presented in differential form; in cumulative form, the index values are 1 less. Values $s < 2$ ($s_r < 4$) indicate that the larger (massive) particles contain most of the mass of the particle ensemble, while values $s > 2$ ($s_r > 4$) indicate that most of the mass is concentrated in small particles.

The mass spectrum of fragments formed as a result of destructive collisions between solid bodies was examined in many studies. According to models [166–169], the mass spectrum index of asteroid fragments formed during a high-speed impact is $s = 1.7-2$. Important information is provided by laboratory and natural experiments. Experimental studies of the destruction of solid bodies during high-speed impacts were conducted to explore the collisional evolution of asteroids and to model their fragmentation during impacts. Many experiments were carried out on the impact of a smaller body (the impactor) on a larger one (the target) to study the masses (sizes), shapes, velocities, and rotations of the fragments formed as a result of the destruction of the target (see review in [170]). Experimental studies were conducted for various shapes, sizes, structures, and materials of the target (basalts, gypsum, pyrophyllite, ceramics, cement mixtures, glass, artificially created conglomerates, meteorite samples — ordinary and carbonaceous chondrites) and for various velocities, shapes, and materials of the impactor. According to [171], based on the results of most experiments, the values of s are in the range of 1.65–1.88 and, consequently, s_r is in the range of 2.95–3.64. According to the results of the DART experiment, the spectrum of ejected particles is described by $s_r = 2.7 \pm 0.2$ [158]. According to review [171], dust and meteoroid particles colliding with Earth are described in the range of masses of less than 1 g by a spectrum of sizes with an index s_r of 3.2. Given this spread, when modeling particle ejection upon impact, $s_r = 3.3$ can be considered a certain estimated average value. It is apparent that, for $s_r > 3$, the cross-sectional area of the particle ensemble increases with decreasing r, and the total contribution of small particles (under the condition $x \equiv 2\pi r/\lambda \geqslant 1$) to the scattering of the solar radiation flux becomes more significant.

Small particles are ejected with higher velocities than larger particles. Similar to the mass and size spectra of particles, many researchers use a power-law relationship between the size (radius) r of particles ejected by impact and the ejection velocity v in the form $v(r) \propto r^{-\beta}$. In [148], models and experiments on determining the velocity spectrum of fragments formed by high-speed impacts are reviewed, and some average value of $\beta \approx 0.5$ is given.

Small particles are scattered after ejection relatively quickly due to their relatively high velocity, so a significant increase in the brightness of the object (asteroid) due to the appearance of a dust coma and the subsequent decline in brightness occur on a short time scale. Larger particles also form near-asteroid structures (for example, tails), which make a more modest contribution to the overall brightness, but this contribution decreases with time much more slowly. An example is the light curve of the binary asteroid 65803 Didymos during the collision with the DART spacecraft, shown in Fig. 2 in [172]. The appearance of a coma of the fastest (small) particles generated a 'flash' on a time scale of $\sim$ 10 min. Larger particles are ejected at lower speeds, and an ensemble in the form of a 'tail' was formed from them, which then dispersed relatively slowly (over several weeks) along the orbit and formed a meteoroid stream. Note that the characteristic time of dispersal of the dust coma depends on the size of the object, since the dispersal speeds of dust particles of a given size are virtually the same for targets of any size. The dispersal time is, in the first approximation, approximately proportional to the size of the target asteroid, and, for a body $\sim$ 100 km in size, the dispersal time can be as long as several days.

3.3 Critical energies of mechanisms for initiating sublimation-driven dust activity of asteroids using example of asteroid 145 Adeona and frequency of sublimation-driven dust activity in ensemble of asteroids

We consider the conditions under which the SDA of an asteroid can become detectable. It is clear that, since the relative change in the brightness of an object is measured, the number of ejected particles generating the SDA phenomenon should be greater for larger bodies. Therefore, the analysis should be carried out for a specific class of asteroid sizes. The observations described above (see Table) were carried out for asteroids with a size of $\sim$ 100 km.

Study [145] examined the application of the results of the above analysis to a specific asteroid 145 Adeona of taxonomic class C. Observations of the asteroid are discussed in Section 2.1. For convenience and logical coherence of presentation, we partially repeat some necessary information about the asteroid. According to [173], the diameter of this asteroid $D_t = 144$ km, density $\rho_t = 1520$ kg m^{-3}, and albedo is 0.048. The presence of a sublimation-driven dust exosphere near asteroid 145 Adeona was discovered in September 2012, one year (or $\sim$ 0.25 of the orbital period) before passing perihelion [65]. The increase in the reflectivity of 145 Adeona in September 2012 compared to 2004 was, in the B band, 21.7% (see Fig. 5). Although the contribution of reflection from the dust component is usually estimated using the R band, the use of the B band for such an assessment made it possible to show at a qualitative level the predominance of small ($\sim$ 0.1 μm) particles in the dust exosphere of 145 Adeona. Later (in 2021) observations of asteroid 145 Adeona (see Fig. 9) also showed an increase in the reflectivity in the B band compared to 2004, but that time it was $\sim$ 10%.

To assess the photometric features, we introduce a factor γ of variation in illumination created on Earth by the asteroid in the visible part of the spectrum due to the ejection of dust and the formation of a light-reflecting dusty exosphere. As noted above, for 145 Adeona in the B band, $\gamma \simeq +0.1$. This implies that the number of solid particles ejected into the near-asteroid space should provide an increase in the light energy reflected by the asteroid + dust exosphere system by a factor of $(1 + \gamma)$. We consider both of the above-mentioned variants of the mechanism for the appearance of dust matter in the vicinity of the target asteroid: (1) ejection upon impact

(collisional mechanism) and (2) comet-like activity of ice-containing layers exposed upon impact (collisional-sublimation mechanism).

3.3.1 Collisional mechanism. We make a simple estimate of the required ejection mass in the collisional mechanism, based on the change in the optical characteristics of the object. We introduce the concept of the optical cross section of an asteroid defined as a product of the geometric cross section of the asteroid and its reflectivity (albedo), i.e., $0.25 \times \pi D_t^2 A_t$, where D_t is the diameter of the asteroid, and A_t is the albedo of its surface. The geometric albedo is usually employed as the albedo of planets, asteroids, etc. We calculate the optical cross section of an ensemble of dust particles under the assumption that it is equal to the sum of the optical cross sections of the dust particles, i.e., the sum of the geometric cross sections of the dust particles multiplied by the reflectivity of A_d dust particles. Since we are dealing with small particles (the size is commensurate with the wavelength), the concept of geometric albedo in the usual sense is no longer applicable here. Nevertheless, as shown by a comparison of the absolute stellar magnitudes of dust grains consisting of amorphous carbon with a radius of $r = 0.09$–2.8 μm, calculated using the exact theory (see [130], in particular, Fig. 5 from the cited work), using the 'geometric' approximation of the optical cross section of the dust grains, the optical cross sections can be represented in a wide range of phase angles ($0-40^\circ$) as $A_d \pi r^2$, where $A_d = 0.092$. This value is twice the albedo A_t of asteroid 145 Adeona. Note that study [174], based on cometary dust polarization models, has shown that the reflectivity of the dust can be several times higher than the standard value (for the comet nucleus). Since relative changes in the reflectivity spectra of asteroids are considered here, a parametric approach with A_t/A_d as a parameter can be used. For asteroid 145 Adeona, $A_t/A_d = 0.5$ can be taken.

To justify the simplified approach to the analysis of the reflective properties of the dust particle ensemble — the dust exosphere of the asteroid — it is also of importance to note that the conditions necessary for such an approach are fulfilled: the optical thickness of the dust layer is small (less than ~ 0.3) and the particles are 'independent,' i.e., the distance between the particles is sufficiently large (exceeds three particle sizes) [175].

As noted above, the size distribution of (dust) particles is usually represented as $\mathrm{d}n(r) \propto r^{-s_r}\,\mathrm{d}r$, where r is the particle radius. Study [176], based on observations of comet 67P/Churyumov–Gerasimenko, found that $s_r = 4$ for large particles and is smaller for small particles. A similar trend is discussed in [177]. It is noted that, in the coma of comet 81P/Wild, the distribution of dust particles sized from 0.1 to 10 μm is described by $s_r = 2.89$; however, for larger particles, s_r is significantly higher. It should be noted, however, that the spectrum of the sizes of the smallest particles is a quantity that rapidly changes after the ejection, since dynamic effects that distort (reduce) the initial (at the moment of separation of the particles from the parent body) value of s_r affect small particles much faster and more strongly. In general, as already noted in Section 3.2, for further estimates, we can adopt $s_r = 3.3$ for small particles. This distribution qualitatively correctly specifies the main contribution to scattering by submicron and micron particles. More specifically, in the following discussion, we take $s_r = 3.3$ for dust particles with a radius of 0.1 to 10 μm and $s_r = 4$ for larger particles.

The total area S_d of the optical cross section of all dust particles in the size range $r_{min} - r_{max}$ can be obtained from

$$S_d = C \int_{r_{min}}^{r_{max}} r^{-3.3} A_d \pi r^2\,\mathrm{d}r = \frac{1}{0.3}\, C\pi A_d \left(\frac{1}{r_{min}^{0.3}} - \frac{1}{r_{max}^{0.3}} \right). \tag{8}$$

Here, $r_{min} = 0.1$ μm, $r_{max} = 10$ μm. For even smaller dust particles, whose dimensions are significantly smaller than the wavelength, the scattering efficiency in the visible range of the spectrum is very small (see, for example, [115]), and the contribution of this component of dust to optical characteristics can be ignored. For $r_{max} \gg 10$ μm, the value of S_d is virtually independent of r_{max}. Equation (8) clearly shows that the main contribution to S_d is made by small particles. The scattering area of 0.1–10-μm dust particles is more than 4 times larger than that of all particles larger than 10 μm, and the contribution of large particles can also be ignored.

We now estimate the mass of ejected dust M_d required to provide a given ratio γ of the total optical cross-section area of dust particles to that of the asteroid. From the relation $S_d = \gamma \times 0.25\pi A_t D_t^2$, we find C to obtain

$$M_d = C \int_{r_{min}}^{r_{max}} r^{-3.3}\, \frac{4}{3}\, \pi r^3 \rho_d\,\mathrm{d}r \approx \frac{\pi}{3}\, \gamma D_t^2 \rho_d\, \frac{A_t}{A_d}\, r_{min}^{0.3}\, r_{max}^{0.7}. \tag{9}$$

Assuming $A_t/A_d = 1/2$, $\gamma = 0.1$ and $\rho_d = 1500$ kg m^{-3}, we obtain from this formula for Adeona $M_d \simeq 1.6 \times 10^3$ t. The total mass of the ejecta is, of course, larger. Equation (9) is not applicable to estimating the total mass of the ejecta, since, as was indicated above, in the size range $r > 10$ μm $s_r \approx 4$, and the dependence of M_d on r_{max} becomes much weaker (proportional to $\ln(r_{max}/r_{min})$). With a characteristic size of the largest particles of ~ 1 m, the total mass of the ejecta is approximately an order of magnitude greater ($\sim 1.8 \times 10^4$ t). Using the characteristics of asteroid 145 Adeona as a target, we estimate the volume of the ejected substance. It corresponds to the volume of a conical crater with a diameter of 42 m and a depth of 8 m. According to (5), with the 'average Martian' value of $Y = 5$ kPa adopted for 145 Adeona and the impactor density equal to the density of the target, we find that, to form such a crater, for example, a collision with an impactor with a radius of 0.82 m at a speed of 4.5 km s^{-1} is necessary. The kinetic energy of such an impactor is 3.5×10^{10} J. This value can be considered 'critical' for the collision mechanism, i.e., minimally sufficient for the dust ejected upon impact to create a picture of sublimation-driven dust activity on the scale observed on asteroid 145 Adeona. Below, for the magnitude of the critical energy of the impactor, we use the notation $E_{p,crit}$.

3.3.2 Collisional-sublimation mechanism. As noted above, the cometary (collisional-sublimation) mechanism is supported by the correlation of the activity of some asteroids with their orbital position in the perihelion region. The number of orbital periods during which an asteroid maintains activity may be greater than one (for 145 Adeona, SDA was observed in three passes of the perihelion region). We now consider the collisional-sublimation variant in somewhat more detail.

To estimate the size of the crater, or more precisely, the area of the ice-containing surface exposed by the impact, which provides the cometary mechanism for ejecting dust into the near-asteroid space, it is necessary to estimate the rate of

dust ejection from such a surface. The most suitable analogue is comets whose perihelion distances are close to that for 145 Adeona (2.28 AU) and, therefore, the insolation conditions are similar. In [178, 179] data on the dust loss rate for a dozen such comets are presented. The average dust loss rate varies from 2.1 kg s^{-1} for comet 115P/Maury (nucleus size of 2.2 km) to 87.5 kg s^{-1} for comet 8 IP/Wild 2 (nucleus size of ~ 4 km). Orbital parameters of the active asteroid/comet P/2015 X6 [180] are very close to those of asteroid 145 Adeona. This is a small asteroid (size: ~ 1 km), which was losing dust at a rate of 1–1.6 kg s^{-1} at the peak of its activity. The peak values of the dust loss rate (at the perihelion portion of the orbit) are an order of magnitude higher: according to [178, 179], for comet 115P/Maury, it is 45 kg s^{-1}, while for comet 81P/Wild 2, it is 900 kg s^{-1}.

It should be remembered that these data refer to cometary nuclei of various sizes, for which, in addition, the fraction (by area) of the active region(s) can differ significantly. If we assume that half the area of the cometary nucleus is active, the peak specific rate of dust mass loss $\dot{m}_d$ for the comets discussed in the previous paragraph varies from ~ 7 to ~ 20 kg s^{-1} km^{-2}. For most comets, the fraction of the area of active regions is an order of magnitude smaller, and, consequently, $\dot{m}_d$ in active regions is significantly higher. Apparently, it can be assumed that freshly opened ice-containing regions on asteroids are comparable in specific sublimation activity to the active zones of comets. Further, for 'order of magnitude' estimates, we take the value $\dot{m}_d = 50$ kg s^{-1} km^{-2}.

When discussing Eqn (9), it was concluded that, to ensure an increase in the flux of visible solar radiation reflected from asteroid 145 Adeona by a factor of $1 + \gamma$, it is necessary to have $M_d \simeq 1.6 \times 10^3$ t of dust in the asteroid's exosphere. Since the characteristic dynamic lifetime of the dust exosphere is ~ 0.01 year, the dust emission rate should be ~ 5 kg s^{-1} at $\dot{m}_d = 50$ kg s^{-1} km^{-2}, the active surface area should be ~ 0.1 km^2, and, consequently, the diameter of the exposed surface (crater) needed to provide such a rate should be fairly large: $D_c \sim 0.37$ km. The crater depth will be several ten meters. According to Eqn (5), to form a crater of this size on asteroid 145 Adeona, an impactor moving with a velocity of 4.5 km s^{-1} should be relatively large ($r_p \approx 6$ m). The corresponding value of the critical energy for the activation of SDA detectable as a result of the collision-sublimation mechanism is $E_{p,crit} \sim 10^{13}$ J.

3.3.3 Critical collision frequency. The issue of the frequency of sufficiently effective collisions is reduced to that of the frequency of collisions with impactors whose kinetic energy exceeds $E_{p,crit}$ for a given target asteroid. Figure 25 presents the distribution of small (diameter $d_p < 100$ m) MAB asteroids by size and encounter velocities. The size distribution of such asteroids was obtained using the model dependence (shown by the red line in Fig. 22). The distribution of relative velocities is shown in Fig. 21. Based on this information, the distribution (more precisely, the distribution density) of asteroids by diameter and relative velocity $p(d_p, V_p)$ — the normalized (total number of asteroids divided by N_0) number of asteroids in a cell measuring 1 m $\times$ 1 m s^{-1}, centered on the values d_p, V_p — was obtained. It is this distribution that is displayed in Fig. 25 isolines for some given values of the kinetic energy of the impactors are also shown. By integrating $p(d_p, V_p)$ over the area to the right of the specified lines, we obtain an estimated fraction $\phi(> E)$

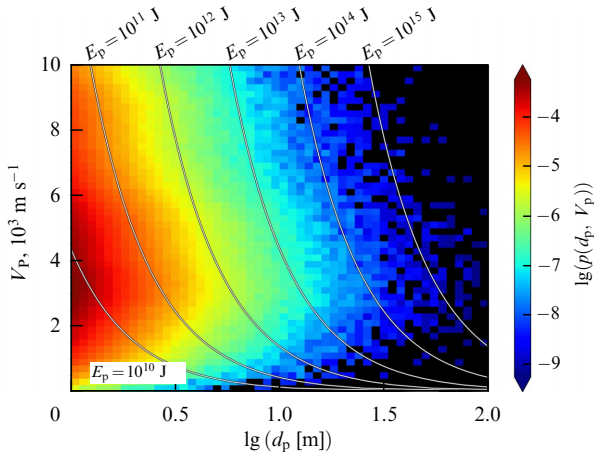

Figure 25. Distribution $p(d_p, V_p)$ of potential impactors by size and velocity. Shown are isolines of kinetic energy of impactors.

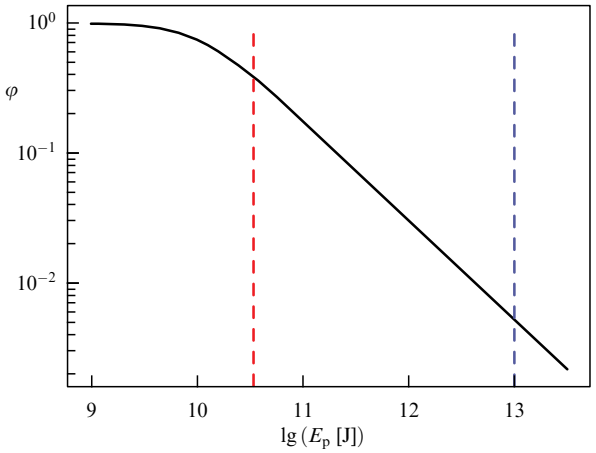

Figure 26. Fraction of ϕ asteroids with (kinetic) energy exceeding E_p. Red dashed line shows critical energy $E_{p,crit} = 3.5 \times 10^{10}$ J. Blue dashed line shows critical energy $E_{p,crit} = 10^{13}$ J (see explanations in text).

of impactor asteroids with an energy greater than the specified value. Figure 26 shows the form of the function ϕ. The lines are shown on which the value of the impactor kinetic energy is $E_{p,crit} = 3.5 \times 10^{10}$ J and 10^{13} J, which approximately corresponds to the critical energy (for the collisional and collisional-sublimation activation mechanisms, respectively) obtained for asteroid 145 Adeona.

According to the MAB asteroid population model (refer again to Fig. 22), the number of asteroids in the diameter range of 1–100 m is $N_0 = 8.4 \times 10^{11}$, and the total number of impactor asteroids with an energy exceeding the critical one is $N_{p,crit} = \phi N_0$. Now, for a specific target asteroid, by analogy with (2), we can determine the rate of collisions with impactor asteroids for which the condition $E > E_{p,crit}$ is satisfied using the formula

$$N_{col}(> E_{p,crit}) = \langle P_i \rangle \pi r_t^2 N_{p,crit} = \langle P_i \rangle \pi r_t^2 \phi N_0 \,. \qquad (10)$$

We now estimate the rate of collisions of asteroid 145 Adeona with bodies (impactors) whose kinetic energy exceeds 3.5×10^{10} J. For $P_i = 21.5 \times 10^{-18}$ km^{-2} $year^{-1}$, we use Eqn (10) to determine that Adeona undergoes $\sim 0.28 \times \phi$ critical collisions per year. For $E_{p,crit} = 3.5 \times 10^{10}$ J in the dependence shown in Fig. 26, we obtain $\phi = 0.4$, and finally

we have for Adeona approximately 0.1 critical collisions per year. The MAB contains approximately 300 large asteroids larger than 100 km, and since the frequency of critical collisions for each of these asteroids is ~ 0.1 per year, at least several dozen objects from this group of asteroids undergo critical collisions in the course of a year. The lifetime of the activity phenomenon is of great importance for estimating the frequency of observed manifestations of SDA. According to the estimate (see Section 3.2), the lifetime of the detectable dust exosphere for a 100-km target is several days (~ 0.1 year). This implies that the expected frequency of observed SDA manifestations due to the collisional mechanism can be ~ 0.3 events per year.

We now estimate the rate of Adeona's collisions with bodies (impactors) whose kinetic energy exceeds 10^{13} J. As noted above, the rate of critical collisions is determined by the factor ϕ. From the dependence shown in Fig. 26, we obtain $\phi = 0.005$ and, consequently, Adeona undergoes $\sim 1.4 \times 10^{-3}$ such critical collisions per year. This value is not very small if we take into account that the duration of the sublimation period, i.e., the period of activity, is $\Delta t \sim 1$ year. So, if all large ($D > 100$ km) primitive asteroids (there are about 200 of them) contain subsurface ice, it can be expected that the frequency of observed SDA manifestations due to the collisional-sublimation mechanism can be ~ 0.3 events per year.

In absolute units, such rates of observed SDA manifestations look underestimated compared to observations (see Section 2.1). This may be due to the number of impactors being underestimated in the discussed model. As can be seen from Fig. 22, the lowest curve is used to describe the population of impactors. According to other models, the number of impactors can be a couple of orders of magnitude higher. Once again, let us recall that the observed manifestations of SDA are only estimated by order of magnitude, since the model uses such important but inaccurately known parameters as s_r, the lifetime of the observed dust exosphere, $\dot{m}_d$, etc. Nevertheless, this is the first attempt to explain the statistics of the observed manifestations of SDA based on physical models.

In our opinion, both collisional and collisional-sublimation mechanisms are applicable to explain SDA manifestations; however, this conclusion requires more precise confirmation in further observations, since the observational statistics are still insufficient, and, of course, more sophisticated models are needed.

3.4 Section conclusions

(1) Dust ejection during asteroid collisions, manifested as asteroid SDA, can be due both to the direct collision of bodies (collisional mechanism) and to the sublimation of ice from the surface, exposed during the impact to ice-containing layers (collisional-sublimation mechanism).

(2) Results of the first attempt to explain the statistics of observed SDA manifestations based on physical models are presented. The models require clarification.

(3) The accumulated statistics of observational manifestations of SDA asteroids are still insufficient to build more precise models. A long-term program of regular observations of SDA asteroids may become a key aspect.

The authors are grateful to the Russian Science Foundation for financial support of the study (grant no. RSCF 22-12-00115).

References

1. Busarev V V, Barabanov S I, Puzin V B *Solar Syst. Res.* **50** 281 (2016); *Astron. Vestn.* **50** 300 (2016)
2. Busarev V V et al., in *48th Lunar and Planetary Science Conf., 20–24 March 2017, Texas, USA* (LPI Contribution, No. 1964) (Houston, TX: Lunar and Planetary Institute, 2017) p. 1919
3. Busarev V V et al. *Solar Syst. Res.* **53** 261 (2019); *Astron. Vestn.* **53** 273 (2019)
4. Shcherbina M P et al. *Nauch. Trudy Inst. Astron. Ross. Akad. Nauk* **7** (1) 93 (2022)
5. Farinella P et al. *Nature* **371** 314 (1994)
6. Gladman B, Michel P, Froeschlé C *Icarus* **146** 176 (2000)
7. Zolotarev R V, Shustov B M *Astron. Rep.* **65** 518 (2021); *Astron. Zh.* **98** 518 (2021)
8. Murray C D, Dermott S F *Solar System Dynamics* (Cambridge: Cambridge Univ. Press, 2000) https://doi.org/10.1017/CBO9781139174817
9. Sharp T G, de Carli P S "Shock effects in meteorites," in *Meteorites and the Early Solar System II* (Eds D S Lauretta, H Y McSween (Jr.)) (Tucson, AZ: Univ. of Arizona Press, 2006) p. 653
10. Goswami J N *New Astron. Rev.* **48** 125 (2004)
11. Ghosh A "Asteroidal heating and thermal stratification of the asteroidal belt," in *Meteorites and the Early Solar System II* (Eds D S Lauretta, H Y McSween (Jr.)) (Tucson, AZ: Univ. of Arizona Press, 2006) p. 555
12. McCoy T J, Mittlefehldt D W, Wilson L "Asteroid differentiation," in *Meteorites and the Early Solar System II* (Eds D S Lauretta, H Y McSween (Jr.)) (Tucson, AZ: Univ. of Arizona Press, 2006) p. 733
13. Schorghofer N *Astrophys. J.* **682** 697 (2008)
14. Rusol A V, Dorofeeva V A *Open Astron.* **27** 175 (2018)
15. Sugita S et al. *Science* **364** eaaw0422 (2019)
16. Westphal A J et al. *Astrophys. J.* **694** 18 (2009)
17. Filacchione G et al., arXiv:2210.02741; in *Comets III* (Eds K J Meech et al.) (Tucson, AZ: Univ. of Arizona Press, 2024) p. 315
18. Chandler C O et al. *Publ. Astron. Soc. Pacific* **130** 114502 (2018)
19. Harris I, Daniel L *Popular Astron.* **58** 93 (1950)
20. Elst E W et al. *IAU Circ.* (6456) 1 (1996)
21. Hsieh H H et al. *Mon. Not. R. Astron. Soc.* **403** 363 (2010)
22. Jewitt D, Hsieh H, Agarwal J "The active asteroids," in *Asteroids IV* (Eds P Michel, F E DeMeo, W F Bottke) (Tucson, AZ: Univ. of Arizona Press, 2015) p. 221
23. Campins H et al. *Nature* **464** 1320 (2010)
24. Rickman H, Gustafson B Å S, Fernández J A, in *Asteroids, Comets, Meteors III. Proc. of a Meeting, AMC 89, Uppsala Univ., June 12–16, 1989* (Eds C I Lagerkvist, H Rickman, B A Lindblad) (Uppsala: Uppsala Univ., 1990) p. 423
25. Fitzsimmons A et al. *Nat. Astron.* **2** 133 (2018)
26. Whitchurch A *Nature Geosci.* **3** 309 (2010)
27. Briani G, Morbidelli A, Gounelle M *Meteor. Planet. Sci. Suppl.* **73** 5241 (2010)
28. Gounelle M, in *European Planetary Science Congress 2012, 23–28 September, 2012, Madrid, Spain*, id. EPSC2012-220
29. Barucci M A, Michel P, in *EPSC-DPS Joint Meeting 2019, 15–20 September 2019, Geneva, Switzerland*, id. EPSC-DPS2019-202
30. Jewitt D, Hsieh H H, arXiv:2203.01397; in *Comets III* (Eds K J Meech et al.) (Tucson, AZ: Univ. of Arizona Press, 2024) p. 767
31. Dones L et al. *Space Sci. Rev.* **197** 191 (2015)
32. Jewitt D *Astron. J.* **137** 4296 (2009)
33. Chandler C O "Chasing tails active asteroid, Centaur, and Quasi-Hilda discovery with astroinformatics and citizen science," Ph.D. Thesis (Flagstaff, AZ: Northern Arizona Univ., 2022); Northern Arizona Univ. ProQuest Dissertations Publ. 29324763 (2022)
34. Greenberg R et al. *Icarus* **135** 64 (1998)
35. Yamamoto T *Astron. Astrophys.* **142** 31 (1985)
36. Snodgrass C et al. *Astron. Astrophys. Rev.* **25** 5 (2017) https://doi.org/10.1007/s00159-017-0104-7
37. Cheng A F *Icarus* **169** 357 (2004)
38. Bottke W F et al. "The collisional evolution of the main asteroid belt," in *Asteroids IV* (Eds P Michel, F E DeMeo, W F Bottke) (Tucson, AZ: Univ. of Arizona Press, 2015) p. 701

39. Bottke W F, Jutzi M "Collisional evolution of the main belt as recorded by Vesta," in *Vesta and Ceres. Insights from the Dawn Mission for the Origin of the Solar System* (Cambridge Planetary Science, Eds S Marchi, C A Raymond, C T Russell) (Cambridge: Cambridge Univ. Press, 2022) p. 250, https://doi.org/10.1017/9781108856324.020
40. Jewitt D et al., in *American Astronomical Society, DPS Meeting #42* (2010) id. 53.03; *Bull. Am. Astron. Soc.* **42** 1072 (2010)
41. Moreno F et al. *Astrophys. J.* **738** 130 (2011)
42. Bodewits D et al. *Astrophys. J. Lett.* **733** L3 (2011)
43. Chapman C R, Mosher J A, Simmons G *J. Geophys. Res.* **75** 1445 (1970)
44. Schorghofer N *Icarus* **276** 88 (2016)
45. Grundy W M, Stansberry J A *Icarus* **148** 340 (2000)
46. Lauretta D S et al. *Science* **366** eaay3544 (2019)
47. Bottke W F et al. *J. Geophys. Res.* **125** e2019JE006282 (2020)
48. Lowry S C et al. *Science* **316** 272 (2007)
49. Granvik M et al. *Nature* **530** 303 (2016)
50. Wiegert P et al., in *American Astronomical Society Meeting #236* (2020) id. 326.03; *Bull. Am. Astron. Soc.* **52** (3) (2020)
51. Ryabova G O, in *European Planetary Science Congress 2008, 21–26 September, Münster, Germany* (2008) id. 226
52. Ohtsuka K et al. *Publ. Astron. Soc. Jpn.* **61** 1375 (2009)
53. Li J, Jewitt D *Astron. J.* **145** 154 (2013)
54. Hui M-T, Li J *Astron. J.* **153** 23 (2017)
55. Ozaki N et al. *Acta Astronautica* **196** 42 (2022)
56. Rennilson J J, Criswell D R *Moon* **10** 121 (1974)
57. Nimmo F et al. *Nature* **447** 289 (2007)
58. Nathues A et al. *Nat. Astron.* **4** 794 (2020)
59. Hamilton V E et al. *Nat. Astron.* **3** 332 (2019)
60. Hainaut O R et al. *Astron. Astrophys.* **563** A75 (2014)
61. Kelley M S P et al. *Nature* **619** 720 (2023)
62. Garrod R T *Astrophys. J.* **884** 69 (2019)
63. Chandler C O et al. *Astrophys. J. Lett.* **892** L38 (2020)
64. Palmer E M et al. *Planet. Sci. J.* **2** 182 (2021)
65. Busarev V V et al. *Icarus* **262** 44 (2015)
66. Housen K R et al. *Icarus* **39** 317 (1979)
67. Busarev V V et al. *Icarus* **369** 114634 (2021)
68. Busarev V V et al. *Solar Syst. Res.* **57** 449 (2023); *Astron. Vestn.* **57** 439 (2023)
69. Sanchez J A et al. *Planet. Sci. J.* **2** 205 (2021)
70. Vachier F, Carry B, Berthier J *Icarus* **382** 115013 (2022)
71. Lazzaro D et al. *Icarus* **172** 179 (2004)
72. Bendjoya P *Astron. Astrophys. Suppl.* **102** 25 (1993)
73. Arredondo A et al. *Icarus* **358** 114210 (2021)
74. Zappalà V et al. *Icarus* **116** 291 (1995)
75. Belskaya I et al. *Astron. Astrophys.* **663** A146 (2022)
76. Avdellidou C et al. *Astron. Astrophys.* **665** L9 (2022)
77. Belskaya I et al. *Icarus* **284** 30 (2017)
78. Tholen D, in *Asteroids II. Proc. of the Conf., Tucson, AZ, March 8–11, 1988* (Eds R P Binzel, T Gehrels, M S Matthews) (Tucson, AZ: Univ. of Arizona Press, 1989) p. 1139
79. Bus S J, Binzel R P *Icarus* **158** 146 (2002)
80. Bottke W F (Jr.) et al., in *Asteroids III* (Eds W F Bottke (Jr.) et al.) (Tucson, AZ: Univ. of Arizona Press, 2002) p. 3
81. Burns R G *Mineralogical Applications of Crystal Field Theory* (Cambridge Topics in Mineral Physics and Chemistry, Vol. 5) (Cambridge: Cambridge Univ. Press, 1993) https://doi.org/10.1017/CBO9780511524899
82. Nesvorný D, Brož M, Carruba V, in *Asteroids IV* (Eds P Michel, E DeMeo, W F Bottke) (Tucson, AZ: Univ. of Arizona Press, 2015) p. 297
83. Novaković B et al. *Celest. Mech. Dyn. Astron.* **134** 34 (2022)
84. Dermott S F, Nicholson P D *Highlights Astron.* **8** 259 (1989)
85. Nesvorný D, Vokrouhlický D *Astron. J.* **132** 1950 (2006)
86. Durda D D, Dermott S F *Icarus* **130** 140 (1997)
87. Licandro J et al. *Astron. Astrophys.* **525** A34 (2011)
88. Rivkin A S, Emery J P *Nature* **464** 1322 (2010)
89. Usui F et al. *Publ. Astron. Soc. Jpn.* **71** 1 (2019)
90. McKay A J, Bodewits D, Li J-Y *Icarus* **286** 308 (2017)
91. Landis M E et al. *Bull. Am. Astron. Soc.* **53** 180 (2021) https://doi.org/10.3847/25c2cfeb.ebd48157
92. Busarev V V et al. *Solar Syst. Res.* **56** 84 (2022); *Astron. Vestn.* **56** 92 (2022)
93. Busarev V V et al. *Solar Syst. Res.* **58** 315 (2024); *Astron. Vestn.* **58** 317 (2024)
94. Lee P *Icarus* **124** 181 (1996)
95. Zank G P, Matthaeus W H *J. Geophys. Res.* **97** 17189 (1992)
96. Kellogg P J, Horbury T S *Ann. Geophys.* **23** 3765 (2005)
97. Malaspina D M et al. *Astrophys. J.* **711** 322 (2010)
98. Busarev V V et al. *Solar Syst. Res.* **58** 715 (2024); *Astron. Vestn.* **58** 724 (2024)
99. Bradley J P, Sandford S A, Walker R M "Interplanetary dust particles," in *Meteorites and the Early Solar System* (Eds J F Kerridge, M S Matthews) (Tucson, AZ: Univ. of Arizona Press, 1988) p. 861
100. Bradley J "The astromineralogy of interplanetary dust particles," in *Astromineralogy* (Lecture Notes in Physics, Vol. 609, Ed. T K Henning) (Berlin: Springer, 2003) p. 217
101. Kolokolova L et al. "Physical properties of cometary dust from light scattering and thermal emission," in *Comets II* (Eds M C Festou, H U Keller, H A Weaver) (Tucson, AZ: Univ. of Arizona Press, 2004) p. 577
102. Güttler C et al. *Astron. Astrophys.* **630** A24 (2019)
103. Petrova E V, Jockers K, Kiselev N N *Icarus* **148** 526 (2000)
104. Kimura H, Kolokolova L, Mann I *Astron. Astrophys.* **407** L5 (2003)
105. Petrova E V, Tishkovets V P, Jockers K *Solar Syst. Res.* **38** 309 (2004); *Astron. Vestn.* **38** 354 (2004)
106. Lasue J et al. *Icarus* **199** 129 (2009)
107. Lumme K, Penttilä A *J. Quant. Spectrosc. Radiat. Transfer* **112** 1658 (2011)
108. Dlugach J M, Mishchenko M I, Mackowski D W *J. Quant. Specrosc. Radiat. Transfer* **112** 1864 (2011)
109. Dlugach J M et al. *J. Quant. Spectrosc. Radiat. Transfer* **205** 80 (2018)
110. Zubko E, Shkuratov Yu, Videen G *J. Quant. Spectrosc. Radiat. Transfer* **150** 42 (2015)
111. Liu L, Mishchenko M I *Remote Sens.* **10** 1634 (2018)
112. Kolokolova L, Nagdimunov L, Mackowski D *J. Quant. Spectrosc. Radiat. Transfer* **204** 138 (2018)
113. Hansen J E, Travis L D *Space Sci. Rev.* **16** 527 (1974)
114. Mishchenko M I, Travis L D, Lacis A A *Scattering, Absorption, and Emission of Light by Small Particles* (Cambridge: Cambridge Univ. Press, 2002)
115. Ysard N et al. *Astron. Astrophys.* **617** A124 (2018)
116. Tishkovets V P, Petrova E V *J. Quant. Spectrosc. Radiat. Transfer* **252** 107116 (2020)
117. Petrova E V, Busarev V V *Solar Syst. Res.* **57** 161 (2023); *Astron. Vestn.* **57** 166 (2023)
118. Mannel T et al. *Mon. Not. R. Astron. Soc.* **462** S304 (2016)
119. Mackowski D W *Appl. Opt.* **34** 3535 (1995)
120. Mackowski D W, Mishchenko M I *J. Opt. Soc. Am. A* **13** 2266 (1996)
121. Mackowski D W, Mishchenko M I *J. Quant. Spectrosc. Radiat. Transfer* **112** 2182 (2011)
122. Warren S G, Brandt R E *J. Geophys. Res.* **113** D14220 (2008)
123. Dorschner J et al. *Astron. Astrophys.* **300** 503 (1995)
124. Li A, Greenberg J M *Astron. Astrophys.* **323** 566 (1997)
125. Mishchenko M I, Travis L D *J. Geophys. Res.* **102** 16989 (1997)
126. Bockelée-Morvan D et al. *Mon. Not. R. Astron. Soc.* **462** S170 (2016)
127. Busarev V V et al. *Icarus* **304** 83 (2018)
128. Hendrix A R, Vilas F *Geophys. Res. Lett.* **46** 14307 (2019)
129. Ivanova O et al. *Mon. Not. R. Astron. Soc.* **525** 402 (2023)
130. Zubko E *Mon. Not. R. Astron. Soc.* **492** 810 (2020)
131. Petrova E V *Solar Syst. Res.* **58** 196 (2024); *Astron. Vestn.* **58** 198 (2024)
132. Mishchenko M I et al. arXiv:1010.1171; *Polarimetric Remote Sensing of Solar System Objects* (Kyiv: Akademperiodyka, 2010)
133. Marsch E *Living Rev. Solar Phys.* **3** (1) 1 (2006) https://doi.org/10.12942/lrsp-2006-1
134. Pinto R F, Brun A S, Rouillard A P *Astron. Astrophys.* **592** A65 (2016)
135. Öpik E J *Proc. R. Irish Acad. A* **54** 165 (1951)
136. Wetherill G W *J. Geophys. Res.* **72** 2429 (1967)
137. Farinella P, Davis D R *Icarus* **97** 111 (1992)

138. Vedder J D *Icarus* **131** 283 (1998)
139. Zain P S, de Elía G C, Di Sisto R P *Astron. Astrophys.* **639** A9 (2020)
140. Yoshikawa M, Nakamura T, in *Asteroids, Comets, Meteors 1993, IAU Symposium 160, June 14–18, 1993, Belgirate, Italy* (LPI Contribution, 810) (Houston, TX: Lunar and Planetary Institute, 1993) p. 322
141. Campo Bagatin A, in *Asteroids, Comets, Meteors, Proc. of the 229th Symp. of the Intern. Astronomical Union, Rio de Janeiro, Brasil August 7–12, 2005* (Proc. of the Intern. Astronomical Union, Vol. 1, Eds D Lazzaro, S Ferraz-Mello, J A Fernández) (Cambridge: Cambridge Univ. Press, 2006) p. 335
142. Díaz C G, Gil-Hutton R *Astron. Astrophys.* **487** 363 (2008)
143. Cibulková H, Brož M, Benavidez P G *Icarus* **241** 358 (2014)
144. Nagasawa M, Ida S, Tanaka H *Earth Planets Space* **53** 1085 (2001)
145. Shustov B M et al. *Astron. Rep.* **66** 1098 (2022); *Astron. Zh.* **99** 1058 (2022)
146. Peña J et al. *Astron. J.* **159** 148 (2020)
147. Davis D R et al. "Collisional evolution of small-body populations," in *Asteroids III* (Eds W F Bottke (Jr.) et al.) (Tucson, AZ: Univ. of Arizona Press, 2002) p. 545
148. Zolotarev R V, Shustov B M *Astron. Rep.* **67** 1019 (2023); *Astron. Zh.* **100** 879 (2023)
149. Harris A W, Harris A W *Icarus* **126** 450 (1997)
150. Hahn G et al., Technical Note, ESA/ESTEC Contract No. 4000106274 (2014)
151. Granvik M et al. *Icarus* **312** 181 (2018)
152. Nesvorný D et al. *Astron. J.* **166** 55 (2023)
153. Nesvorný D et al. *Icarus* **411** 115922 (2024)
154. Nakamura A, Fujiwara A *Icarus* **92** 132 (1991)
155. Adushkin V V, Khristoforov B D *Combust. Explos. Shock Waves* **40** 694 (2004); *Fiz. Goreniya Vzryva* **40** (6) 71 (2004)
156. Melosh H J *Impact Cratering*: *a Geologic Process* (New York: Oxford Univ. Press, 1989)
157. Vincent J-B et al., in *43rd Lunar and Planetary Science Conf., March 19–23, 2012, Woodlands, Texas* (LPI Contribution No. 1659) (Houston, TX: Lunar and Planetary Institute, 2012) p. 1415
158. Li J-Y et al. *Nature* **616** 452 (2023); arXiv:2303.01700
159. Housen K R, Holsapple K A *Icarus* **211** 856 (2011)
160. Holsapple K A, Housen K R *Icarus* **187** 345 (2007)
161. Sánchez P, Scheeres D J *Meteor. Planet. Sci.* **49** 788 (2014)
162. Terik Daly R et al. *Nature* **616** 443 (2023); arXiv:2303.02248
163. Moreno F et al. *Mon. Not. R. Astron. Soc.* **515** 2178 (2022)
164. Novikov L S *Vozdeistvie Tverdykh Chastits Estestvennogo i Iskusstvennogo Proiskhozhdenia na Kosmicheskie Apparaty* (Impact of Solid Particles of Natural and Artificial Origin on Spacecraft) (Moscow: Univ. Kniga, 2009)
165. Mandeville J-C, Vedder J F *Earth Planet. Sci. Lett.* **11** 297 (1971)
166. Dohnanyi J S *J. Geophys. Res.* **74** 2531 (1969)
167. Takasawa S et al. *Astrophys. J. Lett.* **733** L39 (2011)
168. Deller J "Hyper-velocity impacts on rubble pile asteroids," Ph.D. Thesis (Canterbury: Univ. of Kent, Intern. Max Planck Research School for Solar System Science, 2015); https://kar.kent.ac.uk/54352
169. Ševeček P et al. *Icarus* **296** 239 (2017)
170. Brykina I G, Egorova L A *Adv. Astron.* **2021** 9914717 (2021)
171. Drolshagen G et al. *Planet. Space Sci.* **143** 21 (2017)
172. Graykowski A et al. *Nature* **616** 461 (2023); arXiv:2303.05548
173. Vernazza P et al. *Astron. Astrophys.* **654** A56 (2021)
174. Zubko E, Videen G, Shkuratov Yu, in *47th Lunar and Planetary Science Conference, March 21–25, 2016, Woodlands, Texas* (LPI Contribution No. 1903) (Houston, TX: Lunar and Planetary Institute, 2016) p. 1145
175. van de Hulst H C *Light Scattering by Small Particles* (New York: John Wiley and Sons, 1957)
176. Fulle M et al. *Astrophys. J.* **821** 19 (2016)
177. Zubko E et al. *Astrophys. J.* **895** 110 (2020)
178. Pozuelos F J et al. *Astron. Astrophys.* **568** A3 (2014)
179. Pozuelos F J et al. *Astron. Astrophys.* **571** A64 (2014)
180. Moreno F et al. *Astrophys. J.* **826** 137 (2016)
181. Combi M R et al. *Icarus* **317** 610 (2019)
182. Bodewits D et al. *Astrophys. J.* **786** 48 (2014)
183. Bodewits D et al. *Astrophys. J. Lett.* **802** L6 (2015)
184. Xing Z et al. *Astrophys. J. Lett.* **893** L48 (2020)